# A proposal to Jefferson Lab PAC51

## A Search for a Nonzero Strange Form Factor of the Proton at 2.5 $(\mathrm{GeV/c})^2$

## I. EXECUTIVE SUMMARY

## A Search for a Nonzero Strange Form Factor of the Proton at 2.5 $(\mathrm{GeV/c})^2$

### A. Main physics goals

The goal of the proposed measurement of the parity violating asymmetry (PVA) at large momentum transfer is to address the following questions:

- How large is the contribution of $s\bar{s}$ quark pairs to the hadron current at $x_{Bj}$=1?
- Is the lattice prediction of the almost zero values of the strange form factors consistent with the experiments?

We propose to measure the PVA for elastic electron-proton scattering by using the highly segmented NPS-type PbWO4-based calorimeter (ECAL) [1] as an electron arm and the segmented iron-scintillator-based calorimeter (HCAL) [2] as a proton arm in coincidence mode, using electron−proton angular and energy correlations for suppression of the inelastic background processes.

### B. The proposed measurements/observables

This experiment will detect the electron and proton in elastic electron-proton scattering. Longitudinal polarization of the electron beam will be flipped to measure the PVA. The beam polarization will be found using Compton and Moller polarimeters. The observed variable is the PVA, which is expected to be about -150 ppm. With a total of 40 days of data taking, the projected accuracy for the PVA is on the level of 6.2 ppm.

### C. Specific requirements on detectors, targets, and beam

The experiment will use detector packages based on the NPS and HCAL components at a luminosity of $1.75\times10^{38}$ Hz/cm$^2$. The experiment is designed for 65 $\mu$A of a 6.6 GeV energy polarized CEBAF electron beam and a 10-cm-long LH2 target.

### D. Resubmission

This proposal is an updated version of the PR12-22-005 [3]. We address the issues identified in the PAC50 report (see the Appendix). The main change relative to the previous year document is the section with detailed Monte Carlo simulation of the experiment. The concept of this proposal overlaps significantly with PR-06-004 to PAC29.

# A Search for a Nonzero Strange Form Factor of the Proton at 2.5 $(GeV/c)^2$


R. Beminiwattha (spokesperson) S. P. Wells, N. Simicevic
*Louisiana Tech University, LA 71272*

D.J Hamilton (spokesperson), O. Jevons, R. Montgomery
*SUPA School of Physics and Astronomy, University of Glasgow, Glasgow G12 8QQ, UK*

C. Palatchi (spokesperson)
*Indiana University, Bloomington, IN 47405*

K. Paschke (spokesperson), S. Ali, X. Bai, G. Cates, P. Gautam,
R. Lindgren, N. Liyanage, V. Nelyubin, R. Richards, X. Zheng
*University of Virginia, Charlottesville, VA 232904*

B. Wojtsekhowski (spokesperson and contact person), A. Camsonne, S. Covrig Dusa, P. Degtiarenko,
D. Gaskell, O. Hansen, W. Henry, D. Higinbotham, D. Jones, M. Jones, C. Keppel,
D. Mack, S. Lassiter, D. Meekins, R. Michaels, B. Raydo, H. Szumila-Vance, A.S. Tadepalli
*Thomas Jefferson National Accelerator Facility, Newport News, VA 23606*

T. Horn
*Catholic University of America, Washington, DC 20064*

E. Cisbani, G. Urciuoli
*Istituto Nazionale di Fisica Nucleare - Sezione di Roma, P.le Aldo Moro, 2 - 00185 Roma, Italy*

E. King, J. Napolitano
*Temple University, Philadelphia, PA 19122*

P.M. King
*Ohio University, Athens, OH 45701*

P.A. Souder
*Syracuse University, Syracuse, NY 13244*

P. Markowitz
*Florida International University, Miami, FL 33199*

E. Brash, P. Monaghan
*Christopher Newport University, Newport News, VA 23606*

T. Hobbs
*Fermi National Accelerator Laboratory, Batavia, IL 60510*

G. Miller
*University of Washington, Seattle, Washington 98195-1560*

J. Lichtenstadt, T. Kolar, E. Piasetzky
*Tel Aviv University, Israel*

G. Ron
*The Hebrew University of Jerusalem, Israel*

D. Armstrong, T. Averett
*College of William and Mary, Williamsburg, VA 23185*

S. Mayilyan, H. Mkrtchyan, A. Mkrtchyan, A. Shahinyan, V. Tadevosyan, H. Voskanyan
*AANL, 2 Alikhanian Brothers Street, 0036, Yerevan, Armenia*

W. Tireman
*Northern Michigan University, Marquette, Michigan 49855, US*

P. Datta, A. J. R. Puckett, S. Seeds
*University of Connecticut, Storrs, Connecticut, 06269, USA*

C. Muñoz Camacho
*Université Paris-Saclay, CNRS/IN2P3, IJCLab, 91405 Orsay, France*

and the NPS collaboration

(Dated: May 21, 2023)

# Abstract

We propose an experiment to measure the parity-violating asymmetry (PVA) in elastic longitudinally polarized beam electron-proton scattering at a momentum transfer of 2.5 $(\mathrm{GeV}/c)^2$. This experiment has the potential to discover a non-zero strange form factor due to much higher momentum transfer than was previously investigated and several times higher relative precision of measuring the PVA.

The proposed measurement of the PVA will allow us to determine or put an upper limit on the strangeness form factors, specifically a combination $G^s_M + \eta\, G^s_E$, with $\eta = (\epsilon G^p_E) \,/\, (\tau G^p_M) \sim 0.32$. The projected statistical uncertainty of the PVA is 4.1% which could be translated to the ratio of statistical uncertainty on that combination to the nucleon dipole form-factor of 8.8%. The result will be used in flavor decomposition of the nucleon form factors.

The coincidence between the scattered electrons and recoil protons detected in the shower counters will be used for the identification of the elastic process on the trigger level. The angular and energy correlations will be measured accurately and used for final selection of the elastic scattering events.

In 45 days of beam time at 6.6 GeV and a 65 $\mu$A beam with 85% polarization on a 10-cm-long liquid hydrogen target, assuming 40 days for production, the parity-violating asymmetry PVA will be measured to a statistical precision of $\pm 6.2$ ppm. This measurement will present an important development in the experimental study of the $s\bar{s}$ content of the nucleon and nucleon form factor flavor decomposition. The structure of the detector setup allows future extensions of this measurement to the quasi-elastic processes on deuterium and a Rosenbluth separation of the $G^s_E$ and $G^s_M$, which would require much more beam time than currently proposed.

## CONTENTS

## II. INTRODUCTION

The investigation of strange form factors (SFF) is one of the most active research fields: see reviews [4, 5]. There are several reasons which justify serious present and future experimental efforts to study SFF. First of all, SFF were never measured before at momentum transfer above 1 $(\mathrm{GeV}/c)^2$, so the observation and potential discovery of non-zero SFF properties will be very important for the deeper understanding of nucleon structure, and it will provide essential input for the development of theory. Other motivations include testing of the links between SFF and the results from polarized DIS lepton and neutrino scattering and testing of the predictions of the effective theory of SFF. Polarized elastic electron scattering on the proton, suggested for measurement of the $s\bar{s}$ content [6–8], has been realized in several experiments [9–12]. In addition, flavor decomposition of the nucleon form factor [13], which allows us to advance our understanding of the $G_E^p/G_M^p$ reduction discovered at JLab with an increase of momentum transfer [14], requires experimental data on SFF.

SFF have been found consistent with zero at low momentum transfer and could be explained by several effects, see e.g. review [15]. The variation of SFF with momentum transfer $Q^2$ is a subject of great interest. One possible hypothesis is that SFF have a $Q^2$ dependence similar to that of the $G_E^n$ form factor but at higher $Q^2$ due to a much larger strange quark mass.

Currently used experimental techniques in studies of PVA in elastic e−p scattering are based on two approaches. The first one is the integration method, used at SLAC in a pioneering experiment [16], and further developed at MIT-Bates in a $^{12}$C experiment [9] and at Mainz in a Be experiment [17]. Two recent experiments based on the integration method are SAMPLE [18, 19] and HAPPEX [10, 20, 21]. The second method is based on counting of the events for different helicities of the electron beam. Two experiments based on the counting method are G0 [11], A4 [12]. The apparatus of G0 had two configurations for detecting only the recoil protons or only the scattered electrons.

At low $Q^2$ both methods achieved very high accuracy; however, measurements at $Q^2$ larger than 0.8 $(\mathrm{GeV}/c)^2$ become less accurate due to growing background and/or statistical uncertainties [11]. **We are proposing to use a counting method in coincidence mode**. A scattered electron and a recoil proton will be detected with a time resolution of a few nanoseconds, tight angular correlations, and effective rejection of the low energy background. Such a technique will allow us to use non-magnetic detectors for both the electron and the proton, cover the almost full solid angle possible for given $\Delta Q^2$ and $Q^2$ and operate at high luminosity. The proposed approach is based on the segmented calorimeters which were used in our previous experiments at JLab at similar beam energy and luminosity. The proposed configuration has an effective electron solid angle near 33 msr, which is about five times larger than the solid angle of a universal magnetic spectrometer such as HRS. We therefore propose a measurement of the PVA asymmetry in elastic e−p scattering at an incident electron energy of 6.6 GeV and central electron scattering angle of 15.5°.

The text of the proposal is organized as follows. In Section III we describe in some details the formalism of the PVA asymmetry and the possible values for SFF. In Section IV we describe the experimental approach. Results of the detailed Monte Carlo simulation of the experiment are presented in Sec. V. In subsequent sections, we present the proposed measurements (Sec. VI), the expected results and beam time request (Sec. VIII), and the technical considerations related to the equipment (Sec. VII). The proposal concludes with a Section IX. Finally, the appendix has the PAC50 report on the original proposal PR12-22-005 and addresses the issues identified in the PAC50 report.

## III. PHYSICS MOTIVATION

### A. Overview

There are several interesting questions that motivate us to explore the measurement of PVA in electron−proton elastic scattering at large $Q^2$:

1. Are SFF non-zero at large $Q^2$?
2. What is the $Q^2$ dependence of the strange form factors?
3. What are the constraints on the proton 3D image imposed by the proposed measurement of the $s\bar{s}$ content?
4. How will SFF impact flavor decomposition of the nucleon FF?

We will discuss to what level of accuracy SFF could be measured at the proposed and other kinematics.

### B. PVA asymmetry

The effect of lepton helicity in photon-hadron reactions was first considered by Zel'dovich [22], who estimated the size of the PVA asymmetry. PVA in electron scattering has become an effect of large interest since the development of the Standard Model. Investigation of the spin sum rule in DIS led to a huge jump in interest in the role of the strange quarks in the nucleon structure. An experimental approach was proposed by McKeown [7] and Beck [8], who demonstrated how to measure SFF by using elastic electron-proton scattering.

The asymmetry $A_{PV}$ in e−p elastic scattering can be expressed as:

$$A_{PV} = -\frac{G_F Q^2}{4\pi\alpha\sqrt{2}} \cdot [(1-4\sin^2\theta_W) - \frac{\epsilon G_E^p G_E^n + \tau G_M^p G_M^n}{\epsilon (G_E^p)^2 + \tau (G_M^p)^2} - \frac{\epsilon G_E^p G_E^s + \tau G_M^p G_M^s}{\epsilon (G_E^p)^2 + \tau (G_M^p)^2}$$

$$+ \epsilon'(1-4\sin^2\theta_W)\frac{G_M^p G_A^{Zp}}{\epsilon (G_E^p)^2 + \tau (G_M^p)^2}] \quad (1)$$

where $G_F = 1.17 \cdot 10^{-5}$ GeV$^{-2}$ is the Fermi coupling constant and $G_{E(M)}^{p(n)}$ are the electric (magnetic) Sachs form factors of the proton (neutron), $\theta_W$ is the weak-mixing angle, $\sin^2\theta_W = 0.2312$, $G_A^{Zp}$ is the neutral weak axial form factor of the proton, and $\tau$, $\epsilon$, and $\epsilon'$ are kinematic parameters:

$$\tau = \frac{Q^2}{4M_p^2} \sim 0.72,\ \epsilon = \left[1 + 2(1+\tau)\tan^2(\theta/2)\right]^{-1} \sim 0.94, \text{ and } \epsilon' = \sqrt{\tau(1+\tau)(1-\epsilon^2)} \sim 0.15 \quad (2)$$

The values of the first, second, and fourth terms in parentheses in Eq. 1 are: 0.075; 0.542; 0.038. The third term is zero in the absence of strangeness. For this tree-level calculation, $A_{PV} = -150$ ppm. If the $G_M^s = 0.0042$ (0.088 of $G_{\text{Dipole}}$) or $G_E^s = 0.013$, the third term will be -0.027 and $A_{PV}$ changes by the proposed statistical uncertainty of 4.1%. The value of $A_{PV}$ is the subject of electroweak radiative corrections which are considered in a number of papers, see e.g. Refs. [15, 23].

The second term in Eq. 1 could be also presented as:

$$\left[1 + \frac{\epsilon}{\tau} R_n R_p\right] \sqrt{\frac{\sigma_n}{\sigma_p} / \left[\left(1 + \frac{\epsilon}{\tau} R_p^2\right)\left(1 + \frac{\epsilon}{\tau} R_n^2\right)\right]} \quad (3)$$

where $\sigma_{(n,p)}$ are the electron-nucleon elastic scattering cross sections whose ratio was directly measured in several JLab experiments, and $R_{(n,p)} = G_E^{(n,p)}/G_M^{(n,p)}$ are also experimental observables which were measured in the double polarized experiments.

### C. Expected accuracy for the parity violating asymmetry

Assuming 5.3 ppm statistical accuracy for the raw experimental asymmetry (total statistics of 3.6 $\times 10^{10}$ elastic e−p events) we can evaluate the precision for SFF (see calculation of statistics in section VI). Let us evaluate the components of expression 1 at the kinematics of this proposal. At the proposed forward scattering kinematics $\epsilon = 0.94$, $\tau = 0.71$, $\epsilon' = 0.378$, and $\epsilon'(1-4\sin^2\theta_W) = 0.0284$. PVA is sensitive to the combination of strange form factors which could be rewritten as: $G_M^s + \eta\, G_E^s$, with $\eta = (\epsilon\, G_E^p)/(\tau\, G_M^p) \sim 0.32$ at $Q^2$=2.5 (GeV/$c$)$^2$. The measurement of the PVA with an accuracy of 6.2 ppm (4.1%) will lead to a determination of $G_M^s + \eta G_E^s$ to an accuracy of 0.0042 or alternatively to a level of 8.8% of $G_{\rm Dipole}$.

This precision is consistent with the accuracy of measurements for other parameters which contribute to PVA. Table I shows the relative change of the parameters which cause variation of $A_{PV}$ by the same amount as the projected statistical uncertainty. In all cases, the parameters are known to a precision that does not challenge the statistical uncertainty. The $G_E^n/G_M^n$ ratio is currently known at $Q^2$ range 1-3 (GeV/$c$)$^2$ to 8% relative accuracy [24–26] which contributes less than 1% to the uncertainty of the PVA, and the precision on the proton ratio is roughly 10x better [27]. The ratio of proton and neutron cross-sections is known to better than 3% [24, 27] which contributes at a similar level.

Information on $G_A^{Zp}$ at large momentum transfer is also sufficiently accurate, thanks to the studies in the Dyson-Schwinger approach [28–30] (see Fig. 1) , development of the GMDs models [26], and the results from lattice calculation [31]. The remaining uncertainties in $G_A^{Zp}$ due to higher order corrections are currently a subject of active research. The $G_A^{Zp}$ fit relative uncertainty at

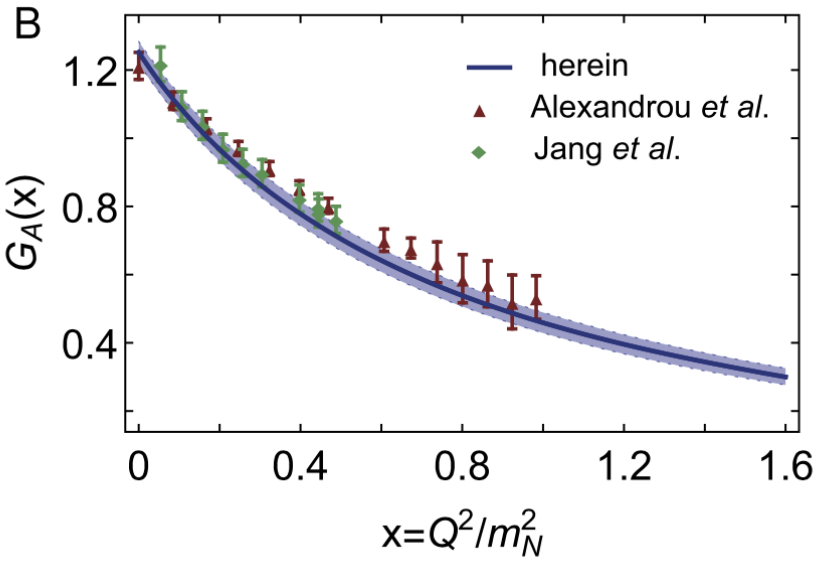


FIG. 1. The axial form factor results from Ref. [28].

2.5 (GeV/$c$)$^2$ is about 3.6% with $g_A = 1.25(3)$ and a mass-scale $M_A = 1.23(3)\, m_N$ [28, 29].

| | Quantity | Absolute | Relative |
|---|---|---|---|
| 1 | Beam energy | 132 MeV | 2.0% |
| 2 | Scattering angle | 0.34 deg | 2.2% |
| 3 | $G_E^n/G_M^n$ | | 38% |
| 4 | $G_E^p/G_M^p$ | | 33% |
| 5 | $\sigma_n/\sigma_p$ | | 10% |
| 6 | $G_A^{Zp}/G_{Dipole}$ | | 70% |

TABLE I. The uncertainties of the parameters in Eq. 1 needed for each contribution of systematic uncertainty to match the $\delta(A_{PV})/A_{PV} \sim 4.1\%$ from the counting statistics.

### D. Counting rate vs. momentum transfer

The measurement of PVA requires accumulation of very large statistics, thus a large solid angle for the detector. Let us present the cross section as a function of $Q^2$:

$$\frac{d\sigma}{dQ^2} = \frac{4\pi\cdot\alpha^2}{Q^4}\cdot\left(1-\frac{Q^2}{2EE'}\right)\frac{E'}{E}\cdot|F^2| \tag{4}$$

$$|F^2| = \left|G_E^p(Q^2)\right|^2\left[\frac{(2-\frac{Q^2}{2ME})^2}{1+\tau}-\frac{Q^2}{E^2}\right]+\tau\left|G_M^p(Q^2)\right|^2\left[\frac{(2-\frac{Q^2}{2ME})^2}{1+\tau}+\frac{Q^2}{E^2}\right]$$

At the proposed kinematics where $\tau \sim 0.71$ we can ignore $Q^2/E^2$, which is just 1/18. The average value of $Q^2$ over the experimental acceptance is dominated by the low $Q^2$ side because of the rapid decrease of the form factors with $Q^2$, so we have to deal with a very simple expression:

$$\frac{d\sigma}{dQ^2} \approx \frac{4\pi\cdot\alpha^2}{Q^4}\cdot\frac{1+\tau\mu^2}{(1+Q^2/0.71)^4}\frac{1-2\tau M/E}{1+\tau} \tag{5}$$

At a given $Q^2$ it is useful to select a range of $\Delta Q^2/Q^2 \approx 0.2$ or a bit less, so the rate variation isn't too large. The exact range of $\Delta Q^2$ will be defined during the design of the apparatus based on considerations such as background rate and detector cost. At the same time, a maximum possible azimuthal coverage is desirable.

### E. Precision vs. momentum transfer

The proposed setup could be used for $A_{PV}$ measurement at several values of $Q^2$ by adjusting the locations of the arms along the beam line. Figure 2 shows the differential cross section $d\sigma/dQ^2$, the integrated cross section in the detector acceptance $d\sigma/dQ^2\cdot 0.2\cdot Q^2$, and a Figure-of-Merit (FOM) $d\sigma/dQ^2\cdot 0.2\cdot Q^2\cdot A_{PV}^2$ vs. the momentum transfer. The drop of the FOM with $Q^2$ is slow ($\propto 1/Q^2$), so the accuracy of the measurement is still quite good, even at 3 $(\mathrm{GeV}/c)^2$. The size of the detector apparatus and the background rates for the proposed kinematics will be discussed in section IV.

### F. Form factors in the GPD approach

A GPD formalism recently developed for the description of the exclusive electromagnetic processes provides a framework for the interpretation of many observables [26, 32, 33]. Form factors of

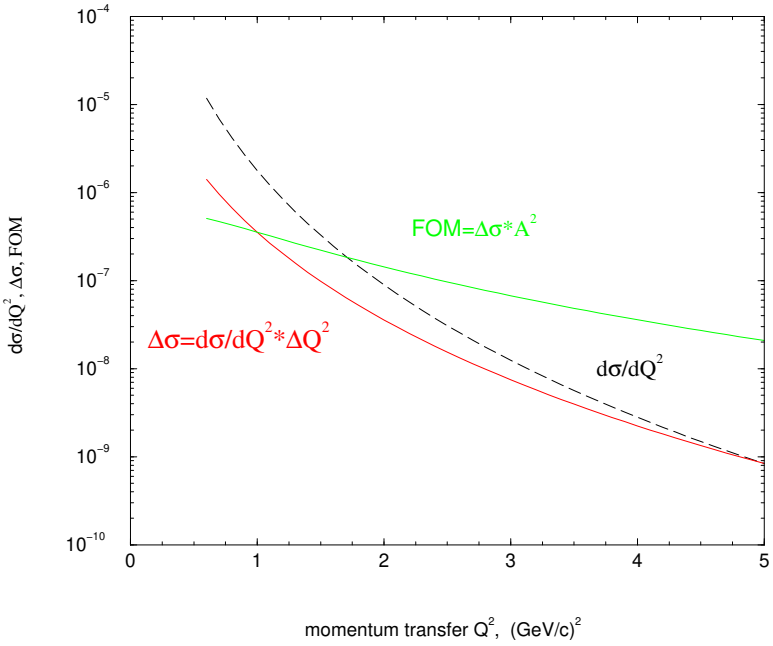


FIG. 2. The differential cross section of e−p elastic scattering at beam energy 6.6 GeV - $d\sigma/dQ^2$, integrated cross section in the detector acceptance $0.2 \cdot Q^2$, and a Figure-of-Merit $d\sigma/dQ^2 \cdot 0.2 \cdot Q^2 \cdot A_{PV}^2$ as a function of $Q^2$.

the nucleon are presented as

$$F_1(t) = \sum_{a=q,\bar{q}} e_a \int_{-1}^{1} dx\, H^a(x,0,t),$$

$$F_2(t) = \sum_{a=q,\bar{q}} e_a \int_{-1}^{1} dx\, E^a(x,0,t).$$

The connection to DIS gives information about GPDs in the limit $t = 0$.

$$H^a(x,0,0) = q^a(x),$$
$$\hat{H}^a(x,0,0) = \Delta q^a(x).$$

The function $E^a$ allows the total angular moment of a quark of flavor $a$ to be determined through Ji's sum rule.

$$E^a(x,0,0) = 2\frac{J^a(x)}{x} - q^a(x),$$

Recent models for GPDs were developed in Ref. [26], in which the GPDs are factorized as a product of a quark distribution $q(x)$, measured in DIS, and an additional function of $x$ and $t$:

$$H_v^q(x,t) = q_v(x)\, \exp\left[t f_q(x)\right],$$

$$q_u^{val}(x) = 1.89\, x^{-0.4}\, (1-x)^{3.5}(1+6x),$$

$$q_d^{val}(x) = 0.54\, x^{-0.6}\, (1-x)^{4.2}(1+8x),$$

where the functions $f_q(x)$ were parameterized and fit to describe the form factors $F_1(t)$ and $F_2(t)$ for the proton and the neutron. The corresponding fits for SFF obtained in Ref. [26] are shown in Fig. 3. Extrapolation from this plot for $G_E^s$ to $Q^2$=2.5 (GeV/$c$)$^2$ suggests a value of 0.01, with a

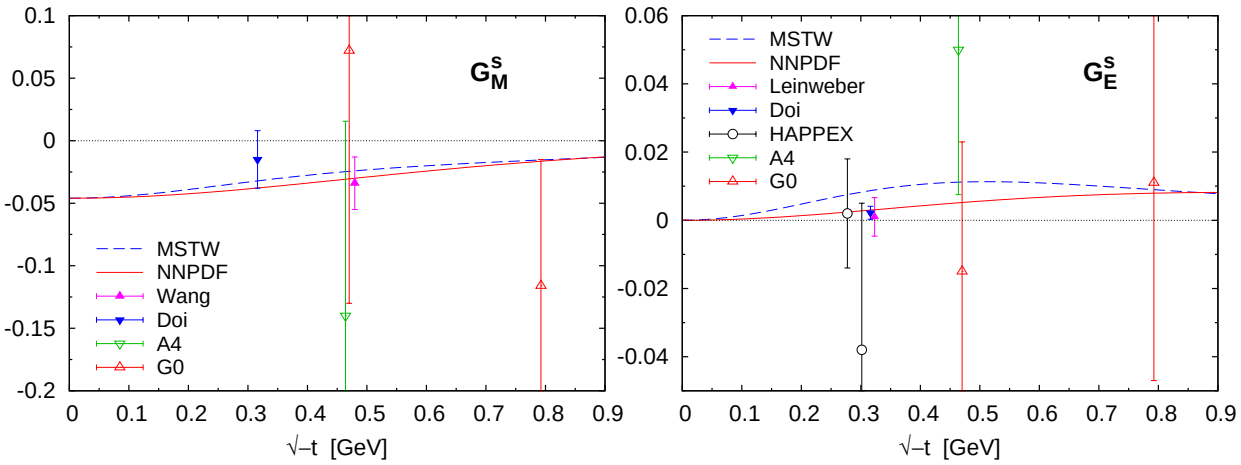


FIG. 3. Fit of strange form factors vs. momentum transfer per Ref. [26].

similar magnitude but opposite sign suggested for $G_M^s$.

### G. Form factor data and SFF

The main trend of $Q^2$ dependence for the electromagnetic form factors at $Q^2$ below 3 (GeV/$c$)$^2$ is described by the dipole formula. From the large mass of the strange quark one can expect that the $Q^2$ dependence of the SFF is weaker compared to the light quark part of the form factors. Because SFF are related to the Z-boson exchange, the probe has a very small size, and the $Q^2$ dependence in the range below 1 (GeV/$c$)$^2$ should be much slower than for electromagnetic form factors, which means that the size of SFF relative to the other electromagnetic form factors must be increasing [34]. In neutrino DIS at $Q^2 = 16$ (GeV/$c$)$^2$ the observed contribution of $s\bar{s}$ is larger than 50% [35], which may indicate that in elastic electron scattering at large $Q^2$ the relative size of SFF could also be large. Finally, published G0 data shown in Fig. 4, indicate a possible rise of SFF with $Q^2$ [11], which must be investigated by measurement of $A_{PV}$ at larger momentum transfer.

The $Q^2$ dependence of the electric form factor of the neutron reflects two competing effects, each of which has its own momentum scale. The scale of $G_E^n$ increase is due to separation between light quarks. This effect is also present in SFF; however, the scale could be shorter or longer, depending on the dominant mechanism. Meanwhile, the decrease is due to the nucleon wave function defined by quark-gluon interaction and interpolated by dipole fit. The decrease of SFF most likely has a similar origin; however, it may have a different scale of $Q^2$. Figure 4 shows the world data and expected accuracy of the proposed measurements.

Significance of the SFF is also illustrated in Fig. 5 for the flavor decomposition of the electromagnetic form factors to $u$- and $d$-quarks (original paper [13] assumed that strangeness contribution to the form factors is zero). Fig. 5 also shows the result of the recent analysis performed by T. Hobbs, M. Alberg, and G. J. Miller on the possible size of the SFF [36, 37], according to which even the value of SFF on the level of $G_D$ is not excluded.

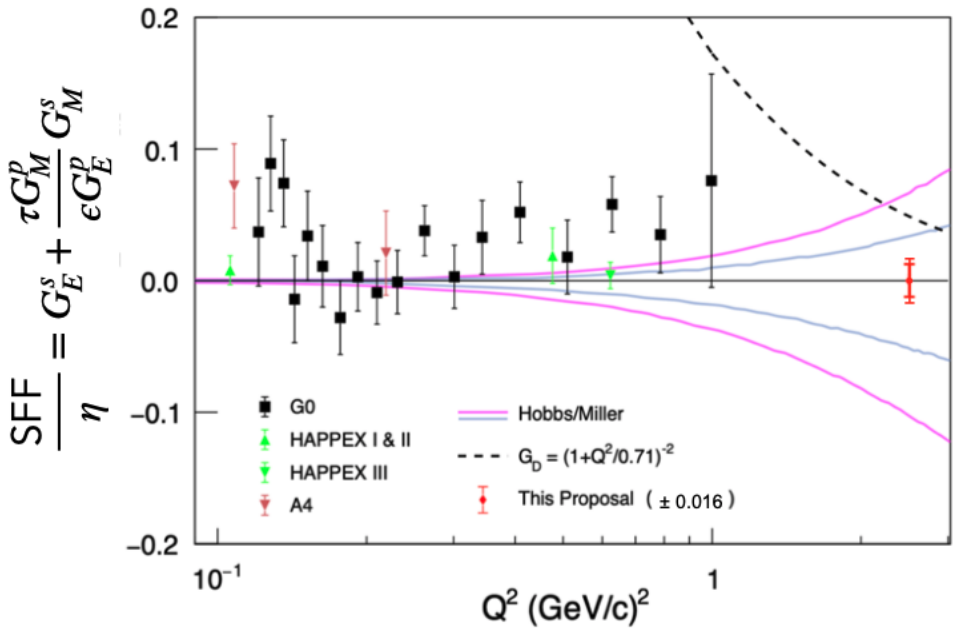


FIG. 4. The strange form factor vs. $Q^2$ according to the G0 experiment [11], HAPPEX, A4 and expected accuracy of this proposal. The blue and pink lines show the area (one sigma) of acceptable value of SFF ($= G_M^s + \eta G_E^s$) according to the analysis in Ref. [36, 37].

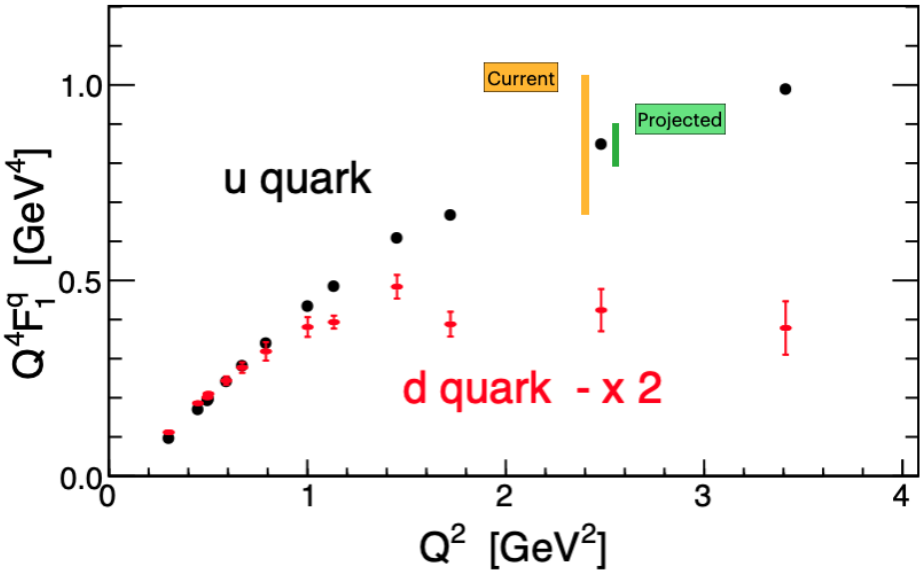


FIG. 5. Flavor separated form factor $F_1$ for strangeness assumed to be zero [13]. Estimated uncertainties for $G_S = G_{Dipole}$ (orange) and max projected from the proposed experiment $G_S = 0.34\ G_{Dipole}$ (green).

## IV. EXPERIMENTAL SETUP

The proposed experiment will study the scattering of polarized electrons from a liquid hydrogen target, as illustrated in Fig. 6. The key considerations of the experimental approach are presented here:

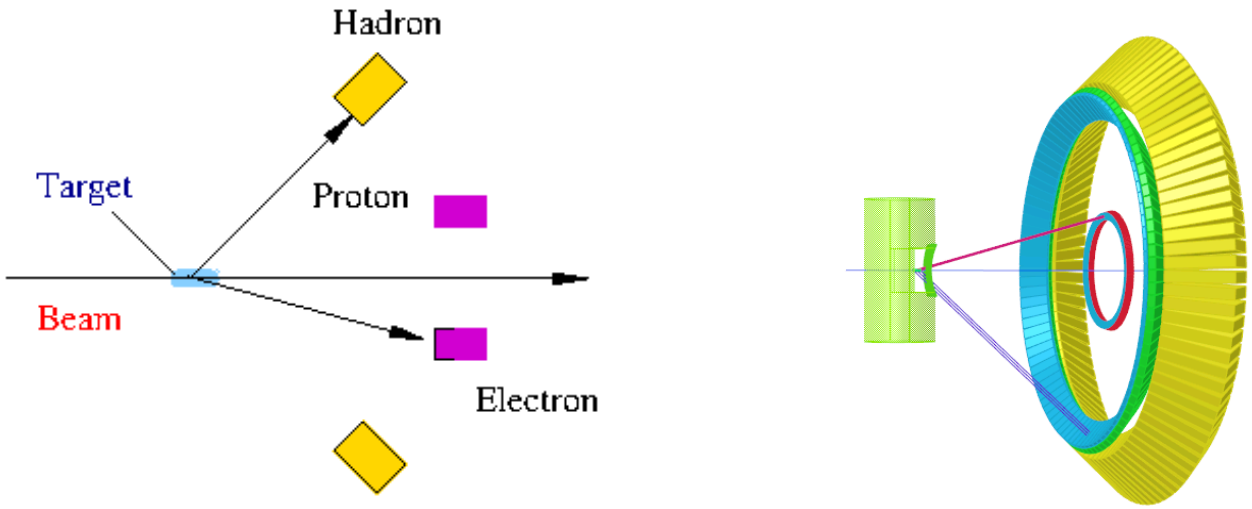


FIG. 6. Schematic of the experimental setup. The target is a 10-cm-long liquid hydrogen. Scattered electrons are detected in the inner ring (electromagnetic calorimeter) and recoil protons are detected in the outer ring (hadron calorimeter).

- Elastically scattered electrons have the maximum kinetic energy among all particles at any given scattering angle.
- Amplitude spectra from an electromagnetic shower calorimeter decrease rapidly, so at a sufficiently high threshold elastically scattered electrons contribute a large portion to the detector rate even at a few $(\mathrm{GeV}/c)^2$ momentum transfer.
- Recoil protons of 1.4 GeV kinetic energy will be detected with high efficiency by a hadron shower calorimeter, even with a relatively large threshold.
- The counting rate at a few $(\mathrm{GeV}/c)^2$ is sufficiently low for the use of the coincidence technique with a segmented detector system.
- Coincidence between the signals from an electron and a proton detector and tight kinematical correlations in azimuthal and polar angles of an elastically scattered electron and a recoil proton allow for a clean selection of elastic events with a simple non-magnetic detector system.
- A non-magnetic detector system based on shower calorimeters allows for the largest solid angle coverage for a given $Q^2$, which is selected based on variation of the counting rate with the scattering angle.
- A large value of $A_{PV}$ allows a precision measurement of SFF at 2.5 $(\mathrm{GeV}/c)^2$ within a modest beam time request of 45 days.

The arrangement of the experiment in Hall C is shown in Fig. 7. The target and scattering chamber need to be moved downstream of the pivot by 3.5 m due to the limited angle range of SHMS (maximum of 36 degrees).

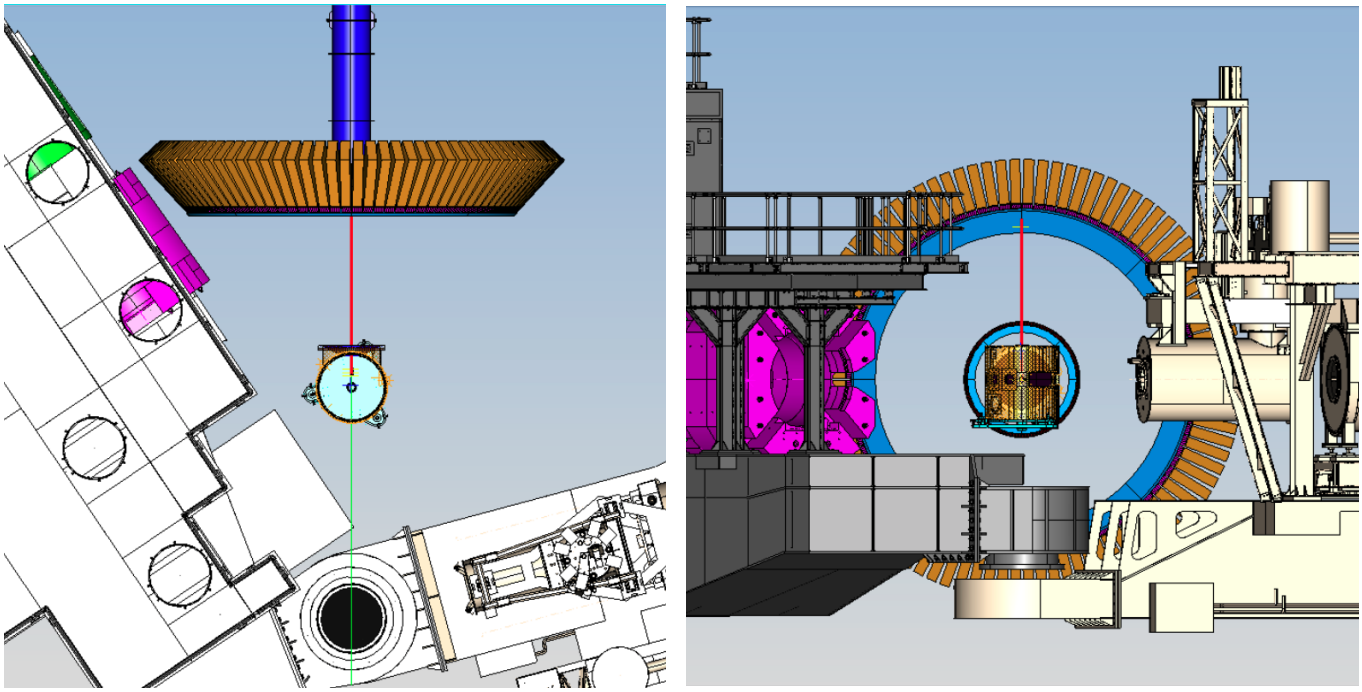

FIG. 7. The geometry of the experiment in Hall C. The top view is shown on the left part of the figure, and the view from the beam dump is shown on the right part of the figure.

### A. Overview

Scattered electrons will be detected in a segmented electromagnetic calorimeter installed at an average polar angle of 15.5±1°, and recoiling protons will be detected in a segmented hadron calorimeter at a polar angle of 42.4±3.5°. Due to the significant length of the target, reconstruction using only the electron arm is not ideal for elastic event selection. Reconstruction will be achieved by a combination of data from both arms. The natural coordinate resolution of the hadron arm of 7 cm will be improved by a pre-shower layer: an array of small plastic scintillator counters behind a two-inch-thick lead wall. These counters will provide a proton coordinate with an accuracy of 0.9 cm. In off-line analysis the electron polar angle will be reconstructed with an accuracy of 0.16° defined by the length of the target. The proton polar angle will be reconstructed off-line with an accuracy of 0.33°, which is mostly due to the target length.

### B. Electron arm structure

Specific geometry of the detector and the DAQ considerations presented here are based on the round shape of the configuration which simplifies discussion of the concept of overlaps. However, it will require adjustment (inserts) due to the rectangular shape of the individual counters, which we omitted on the current level of design. A projected geometry implementation is shown in Fig. 8.

A total of 1200 PbWO4 crystals will be used in the electron arm. They are arranged with a group of five crystals at a given azimuthal angle. Such a group size includes one crystal on each side for

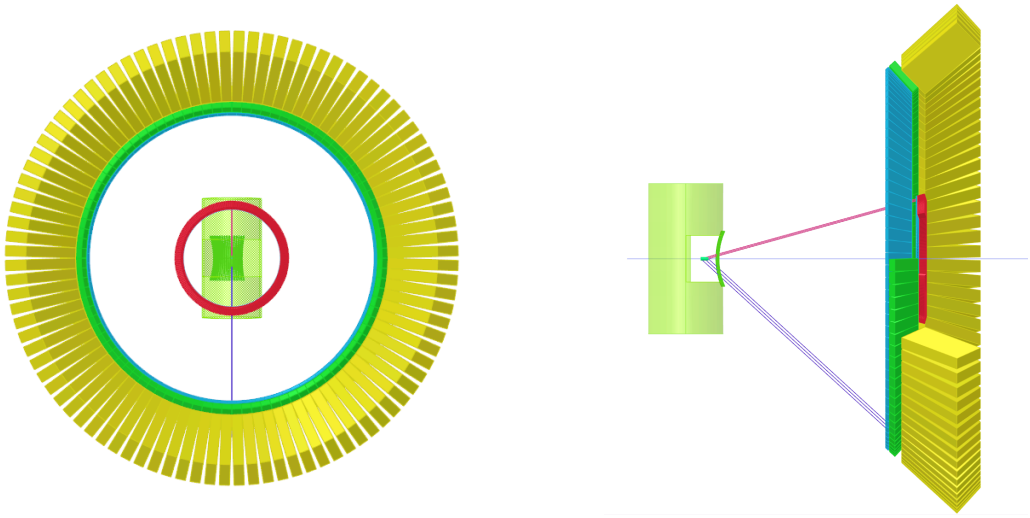

FIG. 8. The geometry of the experiment. In the right-hand figure the beam direction is from left to right. A few detector groups are removed for clarity of the picture.

high energy resolution when an electron hits the inner portion, effectively 1.7 crystals for the required polar angle range of 1.44 degrees, and 1.3 degrees due to the 10-cm-long target viewed at a 15.5 degree polar angle. There are 240 groups of 5 crystals each at the different azimuthal angles. Each crystal group covers an azimuthal angle of 1.5°. Each electron detector has face dimensions 2 cm x 2 cm at a distance from the target of 296 cm. The range of polar scattering angles of the electrons with high energy resolution is defined by a full angular coverage of the detectors of 1.44°, which corresponds to $\Delta Q^2/Q^2 = 0.2$. The solid angle of the electron arm with high energy resolution is 33 msr. The coordinate resolution of the PbWO4 calorimeter is 0.2 cm at 5 GeV. The expected energy resolution at an electron energy of 5.26 GeV is 2.6% (including the effect of a 1-cm Pb shield).

The total rate of elastic events within the high resolution area for the electron arm is 15.5 kHz (with radiative correction included), while the total elastic rate in the full solid angle of the electron detector is 25.5 kHz. For DAQ consideration in the electron arm there are 240 groups, each of them including 5 x 5 counters (25 for every azimuthal group). The azimuthal subsystems have overlaps with adjacent subsystems of two crystals on each side. The trigger of the experiment will be made of an "OR" of the 240 subsystems (after coincidence between an electron subsystem and a corresponding proton subsystem). For each, the threshold will be 4.5 GeV using the VME-based trigger system [38]. Each electron arm DAQ subsystem will cover 7.5° in the azimuthal angle (with 80% overlap) and solid angle of 1.2 msr (for the background counting rate analysis).

### C. The electron calorimeter parameters

The proposed electromagnetic calorimeter (ECAL) has an average radius of 79 cm and consists of 1200 blocks with face dimensions of 2 cm x 2 cm. The ECAL will be constructed from components of the NPS calorimeter [1] and available spares. Such an option will provide superior 2.6% energy resolution for 5.26 GeV scattered electrons and 0.2 cm coordinate resolution. Energy and time resolution are the primary parameters needed for selection of the elastic scattering. An intrinsic time resolution of 1 ns will allow a 40 ns time window on-line and just 4 ns for off-line analysis. The calorimeter will operate at a sub-zero temperature of -20°C. Figure 9 shows the side view of the calorimeter. A 1-cm-thick lead shield will be use for reduction of the radiation dose of the crystals.

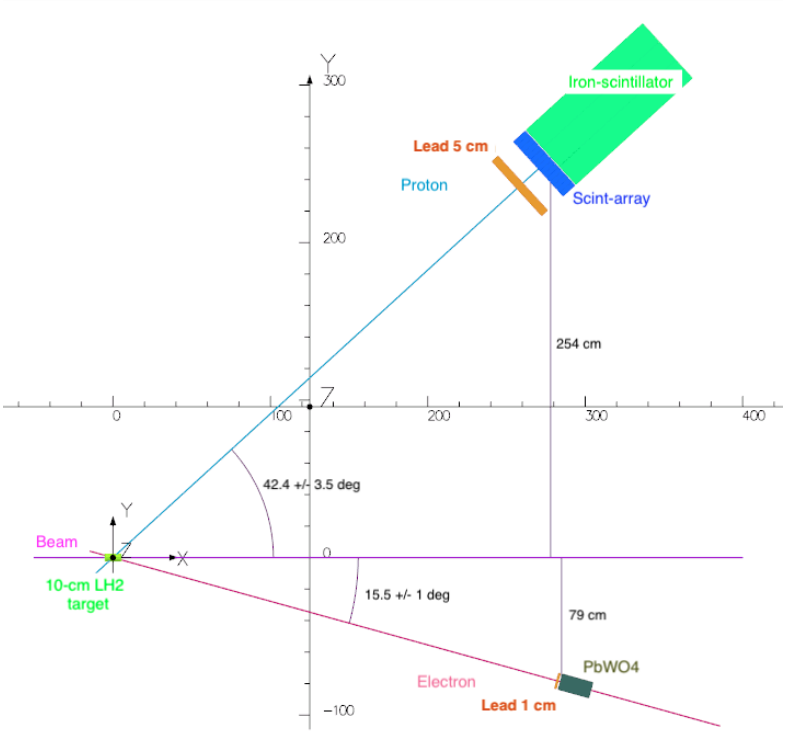


FIG. 9. The geometry of the detector system.

### D. Proton arm structure

A total of 288 iron-scintillator detectors will be used in the proton arm. The calorimeter (HCAL) installed at an average radius of 254 cm. The individual proton detector has face dimensions 15.5 cm x 15.5 cm. The detectors will be located at a distance of 377 cm from the target. Each detector covers a solid angle of 1.7 msr. Detectors will be arranged with three blocks at a given azimuthal angle. This will provide effectively two detectors with full energy/coordinate resolution. The central area will cover the required range of polar angles of 2 degrees (13.2 cm), plus the extra 6.8 cm required due to the 10-cm length of the target viewed at a 42.4 degree polar angle. There are a total of 96 groups of three at different azimuthal angles. For the DAQ of the proton arm we will arrange overlapping subsystems of 3 x 3 detectors in each. There are 96 overlapping DAQ subsystems in the proton arm.

An additional detector of the hadron arm is the highly segmented scintillator hodoscope. Each counter in this array is 3 cm x 3 cm x 10 cm with wave-length shifting fiber for readout by a 64-pixel PMT. It will be protected from the target by a 2 inch wall of lead. Such counters will detect the initial proton with a coordinate accuracy of 0.9 cm. The total number of channels in the scintillator array is 7200, which will require about 113 64-pixel PMTs. The expected cost of PMT H7546B-20 is $3.8k per unit.

### E. The hadron calorimeter parameters

The simple option for the HCAL is iron-plastic plates sandwiched with wave-shifter light collection. Such an option will provide about 60% energy resolution for 1 GeV kinetic energy of the recoil proton. The hadron calorimeter components of the SBS spectrometer could be re-used after completion of the SBS program in Hall A. Figure 9 shows the concept of the proton detector.

### F. The CEBAF polarized electron beam

We assume an incident electron beam intensity of 65 $\mu$A with 85% polarization. Such currents and polarizations have already been delivered using the strained GaAs photoemission electron gun at Jefferson Lab. A raster of the beam will be used to reduce heat density in the target and increase the boiling limit. The Compton and Moller polarimeters will be used to monitor the beam polarization. The projected accuracy of the polarization degree value is 1%, which is a relatively loose tolerance given that recent polarimetry results in Halls A & C have reached well beyond this precision.

A system of BPMs and BCMs developed by the JLab parity collaboration will be used to ensure the helicity-correlated asymmetry in the beam is sufficiently bounded. The requirements of this measurement are relaxed, relative to the relatively high precision, low-$Q^2$ PVA measurements performed over the past two decades at JLab. Standard techniques for the appropriate configuration of the polarized source and the use of an intensity feedback correction to the polarized source will be sufficient.

### G. The hydrogen target

In this experiment we will use the liquid hydrogen target with a 10-cm-long target cell to provide an almost 360° azimuthal aperture for detection of the particles in the forward direction from 14 to 47°. The target will be shifted downstream by 25 cm from the center of the scattering chamber, see Fig. 7. The cylindrical part of the chamber will be a new one with a 60-cm diameter window 10.

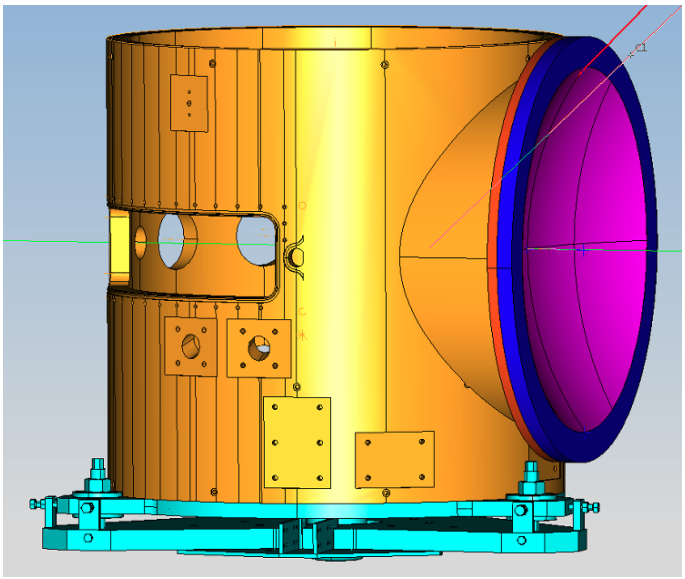

FIG. 10. The CAD model of a new scattering chamber.

## V. MONTE CARLO SIMULATION

### A. GEANT4-based MC code

A simulation of the experimental set-up has been developed within the CERN Geant4 framework [39]. It includes relevant physics interaction models, a realistic description of the experimental geometry and classes for hit digitization, processing and analysis. These efforts have benefited significantly from developments associated with the SBS and NPS Geant4 simulation software codes. The simulated experimental geometry is shown in Fig. 11. It includes the target, scattering chamber, detectors and shielding. In order to study both background and physics events in the three detector systems, the simulation includes event generators for a number of processes:

- A 6.6 GeV rastered electron beam generator for minimum bias background events using the Geant4 physics models for electromagnetic interactions in the target and windows. This does not include DIS and inelastic processes.

- Elastic electron-proton scattering in the $LH_2$ target with form factor parameterizations based on the Kelly fit [40] and radiative corrections from Ref. [41].

- Quasi-elastic electron-nucleon scattering in the aluminum target windows with form factor parameterizations based on the Kelly fit [40].

- Deep inelastic scattering with the CTEQ6.6 PDF parameterization [42].

- Pion electro-production ($ep \to ep\pi^-$ and $ep \to ep\pi^0$) with a cross section parameterization of inclusive electron-proton cross section data by Christy and Bosted [43].

- Pion photo-production ($\gamma p \to \pi^0 p$) with an empirical cross section parameterization derived from JLab E99-114 data [44, 45].

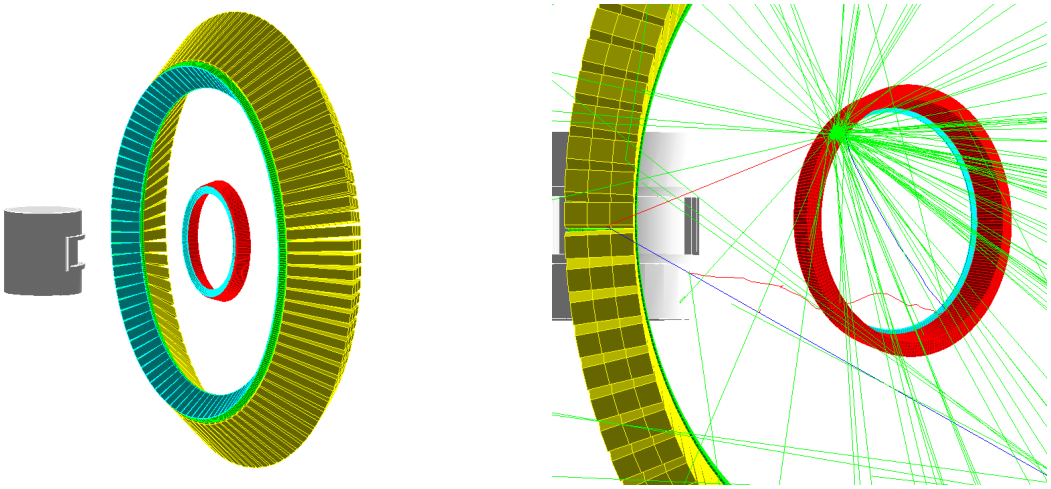

FIG. 11. Two views of the geometry of the experimental set-up as simulated in Geant4. The HCAL blocks are yellow, hodoscope detectors are green and ECAL crystals are red (lead shielding is cyan).

### B. Raw hit and dose rates

Single detector element dose rates for a 65 $\mu$A beam current on a 10 cm $LH_2$ target have been simulated in order to provide a baseline and to optimize the shielding needs of the experiment. Results for simulations with $2 \times 10^9$ primary generated events are shown in Table II. The addition of lead shielding in front of the detectors reduces the raw hit rates by a factor of 6, 4 and 80 for the electron arm, proton arm and hodoscope, respectively. Crucially, the addition of a 1 cm-thick lead shield reduces the electron arm dose rate to 36 rad/hr. This reduction by a factor of almost 30 has been confirmed with dedicated DINREG studies. It leads to a total estimated dose per crystal for 40 days of beam-time of 25 krad, or 3.6 krad in 100 hours of beam on target.

| | Energy deposit rate [MeV/ns] | Dose rate [rad/hr] | Max-to-mean |
|---|---|---|---|
| ECAL | 10.5 | 945 | 3.9 |
| ECAL (with 1 cm shield) | 0.39 | 36.0 | 3.5 |
| HCAL | 0.45 | 0.29 | 4.0 |
| HCAL (with 5 cm shield) | 0.11 | 0.07 | 3.2 |

TABLE II. Single detector element dose rates at 65 $\mu$A beam current for the electron and proton arm detectors (with and without lead shielding in place).

The variation of the raw detector rate as a function of the energy deposit threshold has been studied with Geant4, confirming as expected that the dominant contribution to the rates is from very low energy electromagnetic beam-induced background. This can be seen in Fig. 12, which shows the single detector element energy deposit distributions and rates as a function of the threshold for the three detector types. The maximum energy achievable in simulation for beam-induced background is limited by computational time. For this reason, the corresponding background distributions in ECAL and HCAL are extrapolated to higher energies based on an exponential fit to the lower energy simulated data. With the shielding described above, the estimated rate per detector for an HCAL threshold of 50 MeV is 65 kHz, while hodoscope detectors will see an average rate of 250 kHz with a threshold of 5 MeV. For ECAL, the individual detector threshold will be 500 MeV, which corresponds to a rate of 49 kHz. The implications of these raw rates on pileup, efficiency, and trigger rate are described in the following sections.

### C. Signal pileup and energy resolution

The simulation results on the energy deposit rate in Tab. II allow for an estimation of the base-line shift and fluctuation of the signals at the FADCs. The total energy flow in one crystal of ECAL during a 20 ns time window is 8 MeV. This upper limit for the fluctuation corresponds to 0.2% of the energy of the elastically scattered electron. The equivalent base-line shift for HCAL due to the simulated energy deposit rate of 2.2 MeV corresponds to 2% of the elastic signal. Such fluctuations will not change the energy resolution significantly because the FADC allows for data correction due to pileup. The proposed lead shielding will slightly reduce the calorimeter energy resolution from 2.2% to 2.6% but will have a minimal impact on coordinate resolution.

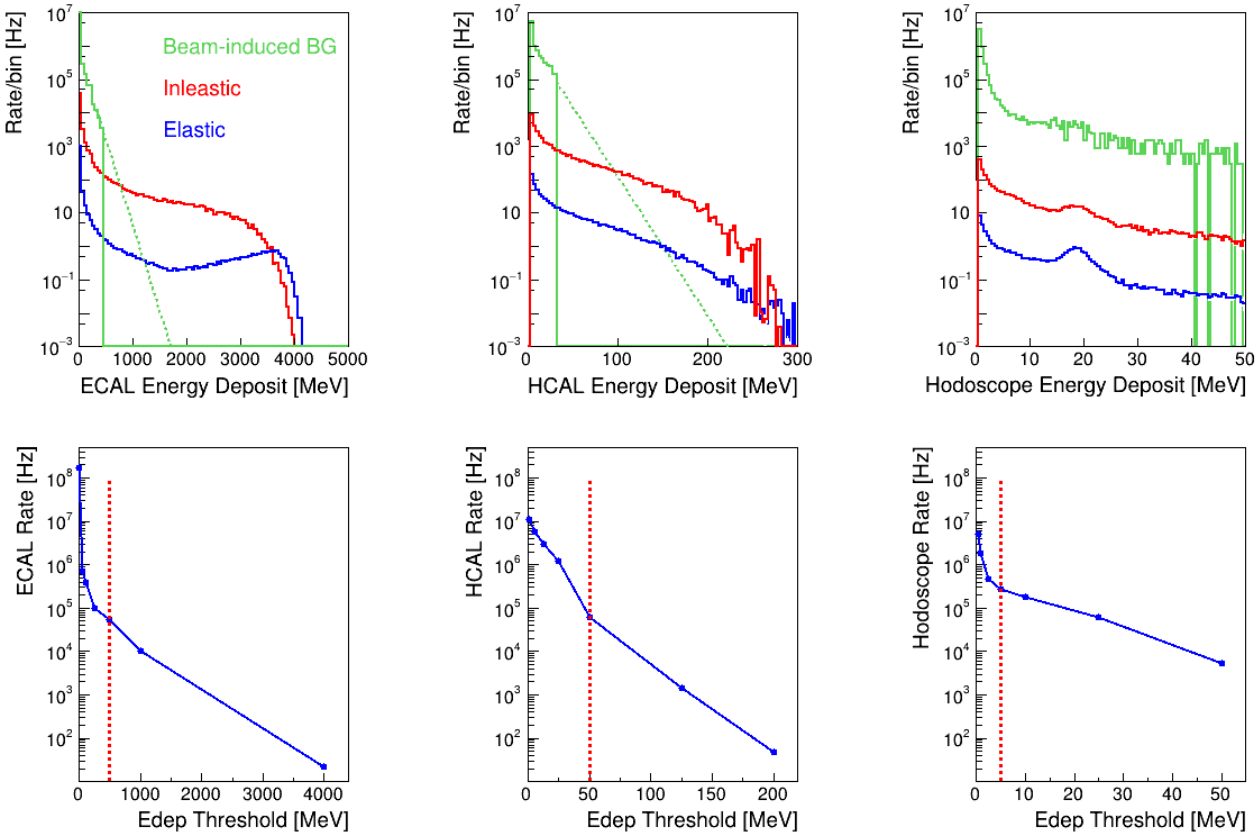


FIG. 12. Energy deposit histograms for individual detector elements (top row, 100 bins in each plot) and graphs of raw single rate at 65 $\mu$A versus energy deposit threshold (bottom row). The colors correspond to MC generator type: green for minimum-bias electro-magnetic processes, red for inelastic processes and blue for elastic scattering. The green-dashed lines show extrapolation of beam background. The red-dashed lines on the graphs show the proposed threshold settings.

### D. Proton detection efficiency

The simulation has also been used to investigate the variation of detection efficiency for both proton detector systems as a function of incident proton energy. As can be seen in Fig. 13, the overall efficiencies are high and improve with increasing kinetic energy. For elastically scattered protons with a kinetic energy of 1.4 GeV, the HCAL efficiency is 97% and the hodoscope efficiency is 87% (where the reduction of the latter is primarily due to charge exchange reactions in the lead shield).

### E. Trigger rates

The trigger will be formed by coincidence between a 5x5 cluster in the ECAL and an element in the corresponding 3x3 block grouping in the HCAL. (This is described in greater detail in Sec. VI.) The ECAL threshold will correspond to an average of 4.5 GeV deposited cluster energy, about 85% of the elastically scattered electron energy. With this threshold, the electron trigger counting rates are dominated by the inelastic event rate, which at the on-line trigger threshold is about 6 times larger than the elastic event rate. The total rate (inelastic plus elastic) is estimated to be around 153 kHz for the full electron arm (1200 counters) as can be seen on the left-hand histogram in Fig. 14

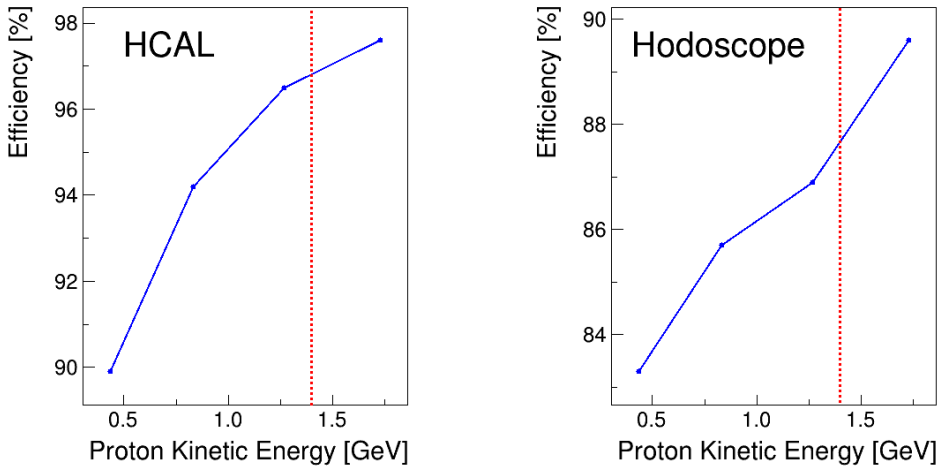


FIG. 13. Detection efficiency as a function of incident proton kinetic energy for HCAL (left) and hodoscope (right) detectors for the thresholds 50 MeV and 5 MeV respectively. The red dashed line corresponds to the momentum for elastically scattered protons in the proposed experiment.

and the elastic rate is 26 kHz. The inelastic rate alone at such a threshold is 127 kHz.

As noted above, the threshold in the proton arm trigger will be 50 MeV, which leads to a high detection efficiency for elastically scattered protons. Using the single detector rate at a 50 MeV threshold as shown in Fig. 12, the HCAL trigger rate is estimated to be at the level of 19 MHz for the full hadron arm (288 counters). The right-hand plot of Fig. 14 shows a comparison of the high-threshold electron arm rate with and without requiring a coincident hit in the corresponding HCAL grouping. The coincident elastic rate is estimated to be 18.3 kHz, which is around 70% of the single electron arm elastic rate.

As described in the next section, the offline analysis will use tighter cuts on geometric correlations and a more restrictive threshold of 5 GeV for the electron arm to exclude inelastic backgrounds. To maintain high resolution, the ECAL acceptance is restricted so that the cluster center should not lie at the edge of the calorimeter. The restricted acceptance, HCAL and hodoscope efficiencies, and $\pm 3\sigma$ angular correlation cuts result in a revised coincident rate of 13.3 kHz. This is the estimated reference *production rate* used throughout this proposal.

### F. Correlated background

The dominant correlated background in this experiment is due to neutral and charged pion electroproduction with detection of the scattered electron in ECAL in coincidence with a charged, energetic hadron in HCAL (referred to as inelastic). Neutral pion photo-production as a result of upstream radiation of a beam electron also contributes, as high energy photons from the pion decay will be detected in the electron arm in coincidence with the recoil proton. There is also a background as a result of quasi-elastic scattering in the upstream and downstream target windows. All four event types have been simulated in Geant4 and a comparison made between the background contamination level for the online trigger condition and realistic more stringent conditions that will be employed in offline analysis.

The online trigger is just a coincidence between the electron and proton arms above their respective thresholds (4.5 GeV and 50 MeV). However in offline analysis, only the high resolution central portion

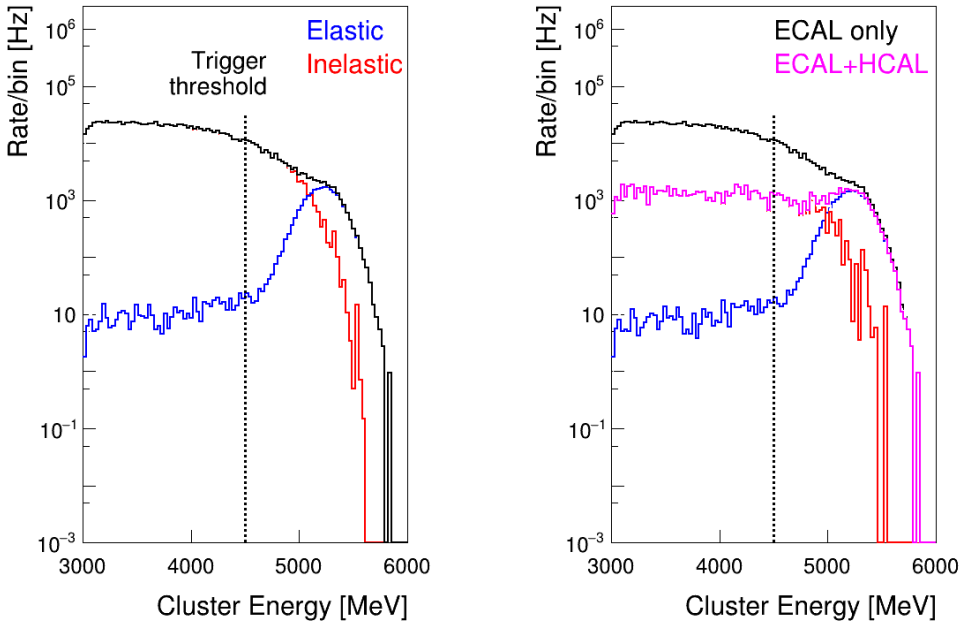


FIG. 14. Simulated rate in the 5x5 crystals subsystem of the electron arm as a function of cluster energy. Both histograms (100 bins) show the contributions from elastic (blue) and inelastic (red) events. The right-hand plot shows the rate with and without a coincident HCAL hit ($> 50$ MeV, magenta).

of ECAL will be considered and cuts will be included on cluster energy ($> 5$ GeV), co-planarity and on the difference between the detected hadron polar angle and the angle expected from the reconstructed scattered electron four-vector (both cuts are $\pm$three sigma or $\pm 0.6^\circ$). The offline position resolution is achieved using the cluster centroid in ECAL and the scintillator hodoscope in the hadron arm. The corresponding histograms for analyzed simulated data are shown in Fig. 15. Integration of these histograms allows for extraction of the fraction of total events for the different coincident event types that were simulated, which are shown in Table III. The inelastic-to-elastic fraction, which is 84.7% for the online conditions, is reduced to 0.2% with offline cuts applied. Correlated background contamination from quasi-elastic scattering in the target windows is around 0.8% of the elastic yield, and neutral pion photo-production is reduced to less than 0.1% of the production rate.

| Fraction of total by event type | Online | Offline |
|---|---|---|
| Elastic scattering | 0.531 | 0.989 |
| Inelastic (pion electro-production) | 0.450 | 0.002 |
| Quasi-elastic scattering (target windows) | 0.015 | 0.008 |
| $\pi^0$ photo-production | 0.004 | 0.001 |

TABLE III. Fraction of total events for the four simulated coincident event types.

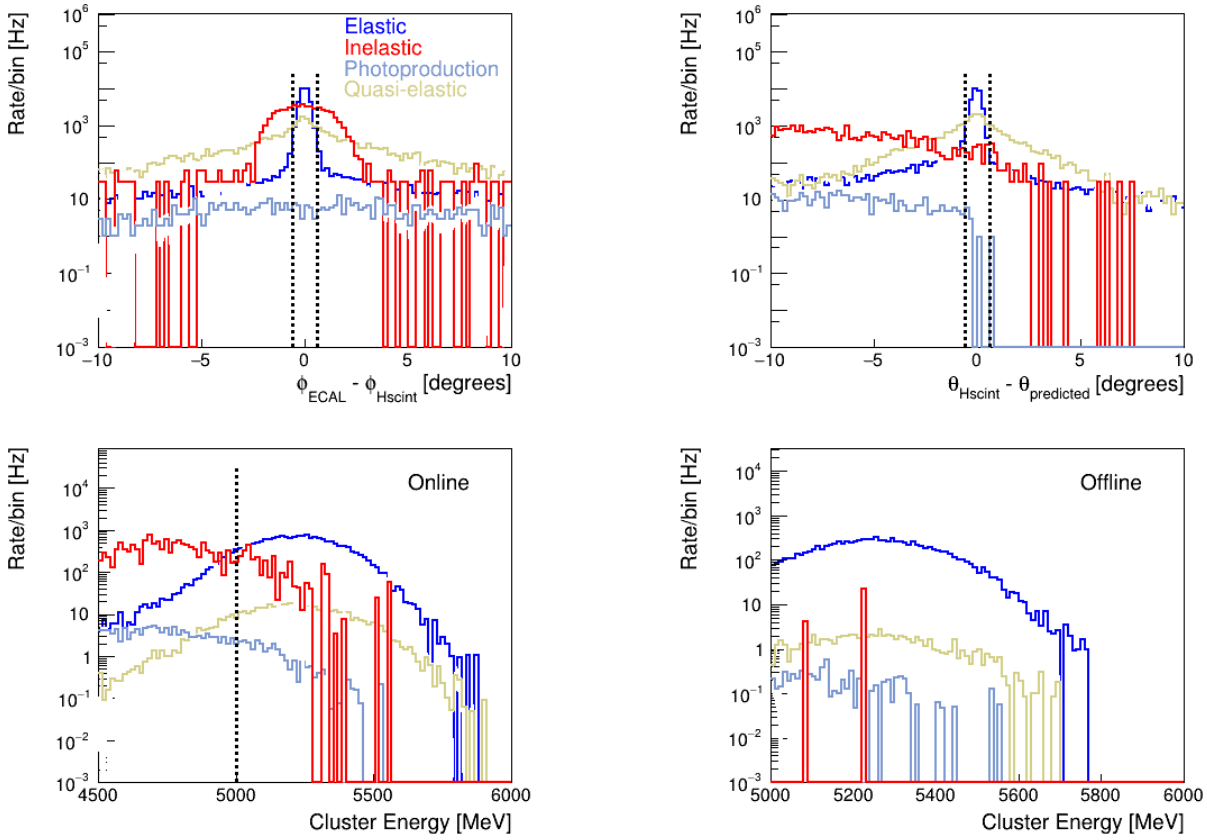


FIG. 15. Histograms for different coincident event types of $\phi_{\mathrm{ECAL}} - \phi_{\mathrm{Hscint}}$ (top left), $\theta_{\mathrm{Hscint}} - \theta_{\mathrm{predicted}}$ and cluster energy for the online conditions (bottom left) and after offline analysis (bottom right). The cuts used in the offline reconstruction are shown as dashed lines.

## VI. PROPOSED MEASUREMENTS

A longitudinally polarized electron beam with a current of 65 $\mu$A at an energy of 6.6 GeV will be used with a 10-cm-long target of liquid hydrogen. The recoil proton will be detected in the hadron calorimeter and an array of small scintillators for better coordinate measurement. The scattered electron will be detected in the highly segmented electromagnetic calorimeter. All features of the experimental technique have been used before at Jefferson Lab and are well developed.

### A. The kinematics and counting rate

The average momentum of the recoil proton will correspond to the elastic scattering of the incident electron with initial energy 6.6 GeV. There is complete overlap of the photon and proton arms. Both cover an almost full $2\pi$ azimuthal angle. The electron arm polar acceptance is $15.5 \pm 0.58^\circ$ for the high resolution area. The proton arm corresponding polar acceptance is $42.4 \pm 2.35^\circ$. If the electron beam energy is a bit less than 6.6 GeV, a slight shift of the electron arm acceptance will be done by moving the detector along the beam direction.

The solid angle of the electron detector for the selected momentum transfer range is 33 msr. The total cross section of elastic electron scattering in the detector acceptance is about 86 pb. At a projected luminosity of $1.75 \times 10^{38}$ cm$^{-2}$sec$^{-1}$ the total rate of coincidence elastic events is 18.3 kHz. With the restricted ECAL acceptance to achieve high resolution, higher ECAL threshold, and tighter offline cuts on geometric correlations, the production rate of 13.3 kHz is estimated. Additional radiative losses are estimated at 20%. With 40 days of production running the statistical error of the raw asymmetry result will be $\pm 5.3$ ppm, and with 85% polarization the PVA will be measured to $\pm 6.2$ ppm.

### B. Detailed trigger structure

Scattered electrons will be detected in a segmented electromagnetic calorimeter installed at an average polar angle of 15.5°, and recoiling protons will be detected in the segmented hadron calorimeter at a polar angle of 42.4°. The rate of each 5x5 electron-arm subsystem will be 2.6 kHz inelastic and about 530 Hz elastic events. A threshold in the proton arm trigger will be at the level of 50 MeV which leads to 97% detection efficiency. The total proton arm rate above 50 MeV is 19 MHz, while the rate of each 32 proton arm subsystem (3x3 blocks) will be 585 kHz. The scintillator hodoscope array is included only in off-line analysis.

We plan to use a 4.5 GeV threshold in the electron arm and a 20 ns time window for coincidence in the on-line trigger logic. Each DAQ subgroup includes 25 electron and 9 proton detectors. As noted above, the total electron arm rate (one subsystem) is 3.2 kHz and the total hadron arm rate (one subsystem) is 0.59 MHz. The projected rate of coincidence of one electron subsystem and one proton subsystem therefore has an accidental rate of 38 Hz and 456 Hz of coincidence events.

In off-line analysis several cuts will be applied: the time window will be reduced to 2 ns (beam RF structure), the coordinate in the electron arm reduced to a central portion of 3 x 1 counters and the coordinate in the proton arm reduced to a central portion of 2 x 1 counters. These changes lead to a reduction in the accidental rate estimate to a value of 0.1 Hz while the elastic rate is 56 Hz. The next step of off-line analysis is applying cuts on scattered electron energy above 5 GeV, co-planarity and polar angle correlations as discussed in Section V. Taking the MC prediction for the inelastic suppression in offline analysis as a result of these cuts, a further reduction of the accidental rate by a factor of around 200 is expected, bringing the real/accidental ratio to the level of $1.1 \times 10^5$.

### C. The systematics

The expected value of $A_{PV}$ at $Q^2 = 2.5$ (GeV/$c$)$^2$ without SFF is -150 ppm. The projected statistical accuracy of the asymmetry value is 6.2 ppm, so the control of systematic uncertainties on the level of 2-3 ppm will be sufficient. Coincidence between the proton and the electron may lead to a new possible source of systematic uncertainty due to acceptance and efficiency correlations; however, it could be greatly reduced by using a proton detector of larger size. The most important systematics are common in the parity experiments, whose collaborations have developed a way to reduce their a level below 0.1 ppm, include:

- beam polarization uncertainty;
- helicity correlated beam position variation;
- helicity correlated beam energy variation;
- helicity correlated dead time of DAQ;
- helicity correlated accidental events.

In the proposed experiment due to large expected asymmetry (150 ppm), the required level of beam related systematics ($\sim$1 ppm) is achievable. The effect of the beam position variation to a large extent cancels out due to the $2\pi$ coverage of the electron detector, so even a very large 100 nm helicity related beam motion on the target would be acceptable for this experiment. Energy variation with helicity flip due to beam intensity and orbit variation will be controlled by means already developed. The raw counting rate of one DAQ subsystem in the proposed experiment is below 2 kHz. Systematics of the dead time correction was one of the serious problems of any counting method until streaming readout was developed. The challenge has been successfully met by the 6 GeV PV-DIS measurement [46], and is under investigation for the very high precision PVDIS measurement planned for SOLID in Hall A.

As shown above, the probability of background events in the collected event sample is relatively low mainly due to high precision in the electron arm energy and tight time and angular correlations between two particles in the event. One background process of concern is the beam helicity asymmetry which appears due the production of hyperons, the significance of which can be calculated from the cross section. Hyperon photo-production occurs at 1-2% of the total inelastic $\gamma-$p cross section, see Ref. [47]. The electro-production of a hyperon occurs at a similar level due to dominance of the quasi-real photon mechanism [48].

For upper limit of contributed asymmetry, we assume the polarization of the hyperon and the effect on the asymmetry in our acceptance are both order 1. However, real coincidence between electron in the ECAL and hadron (from a hyperon decay) in the HCAL is excluded due to low final electron energy in case of hyperon production (less than 4.5 GeV) and high threshold on the final electron energy (5.0 GeV) in analysis and also due to a large mismatch of the polar angles. Hyperons may still enter our event sample through accidental coincidences. In this case, the conservative upper estimate for the asymmetry is $1/(1.1 \times 10^5) \times 0.02 \times 1 =$ **0.2 ppm**.

As seen in Fig. 15, the region of the triggered acceptance which lies outside the elastic peak in dominated by the inelastic contributions. The offline analysis will use the measurements with significant out-of-plane angles and off-elastic polar angle correlations to confirm estimates of the the accepted inelastic background asymmetries. These studies will provide a direct check on the small contributions from hyperon decays.

## VII. TECHNICAL CONSIDERATIONS

### A. Time line of development

We expect that construction of the detector system will be done after completion of a set of approved NPS-based experiments in Hall C and the SBS program in Hall A which use HCAL.

### B. The detectors

The technology and calorimeter detectors themselves already exist, but the holding frames need to be designed. The scintillator array will also use proven technology implemented in, for example, the GEp/SBS CDET detector [49].

The radiation damage affects light transmission in PbWO4 crystals, see e.g. Ref. [50]. The typical reduction of the signal from a GeV energy range electron is about 10-20% after 2 krad dose. A more significant decrease occurs for a high radiation dose as shown in Fig. 16. The signal drops approximately as $[1 - 0.07 \times \log(Dose[rad])]$. Note that the dose shown here was applied by using a beam of high energy electrons, so its distribution in the crystal is close to the profile of the electron shower. Annealing of radiation damage of 3 krad by blue LED light could be done in about three hours [51]. The dose rate in the detectors during the proposed experiment were evaluated using

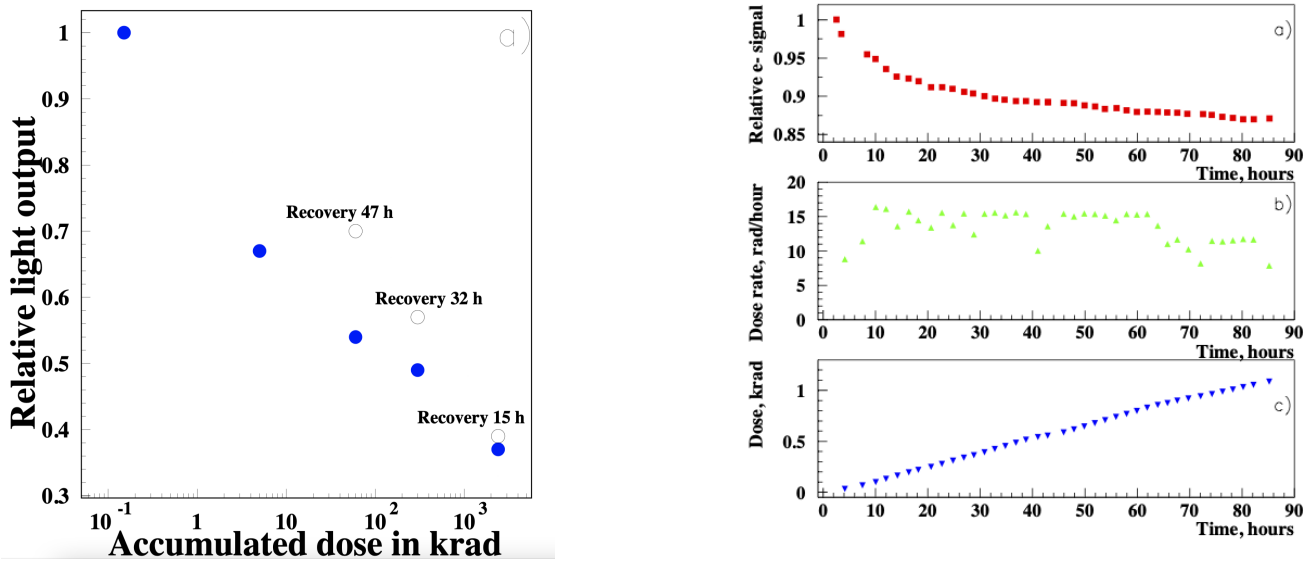


FIG. 16. Left: The signal reduction for the dose in Mrad range. Right: The signal reduction vs. time during irradiation per Ref. [50].

two approaches: a MC in Geant4 framework and a MC in DINREG/GEANT3 framework. The full experiment MC Geant4 calculation results in a mean dose of 36 rad/h for the electron arm crystal, see Table II. It was achieved with the 1-cm thickness lead wall in front of the electron calorimeter, which made reduction of the radiation dose by a factor of 30-40. Results of DINREG MC calculation of the dose are shown in Fig. 17, where the dose varies with depth in the crystal. The level of 150 rad/h corresponds to the maximum of the shower profile (depth of 5-6 cm). The accumulated dose from the latter study is 20 krad per week, which corresponds to average reduction of the signal by 1/3. It could be annealed during weekly accelerator maintenance with the LED-based annealing system

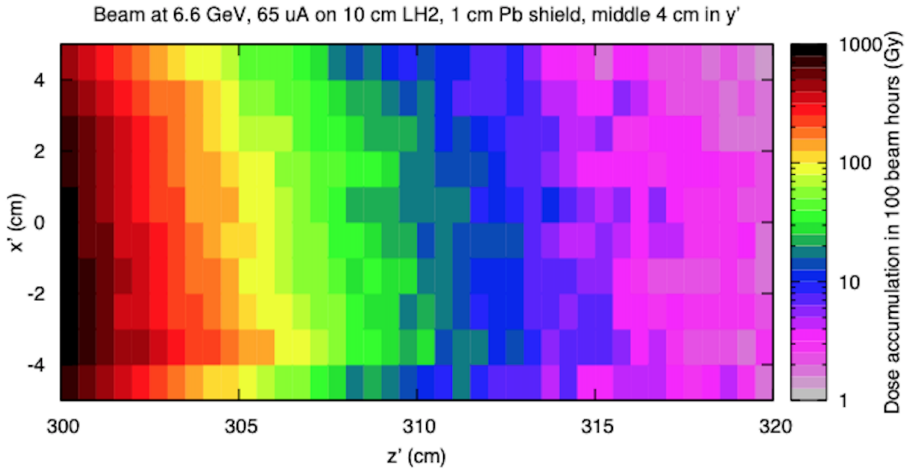


FIG. 17. Radiation dose after 100 hours 65 $\mu$A beam on 10-cm-long LH2 target in the electron arm calorimeter protected by 1-cm-thickness lead wall. Coordinate z=300 cm corresponds to the front face of the calorimeter.

implemented in the NPS calorimeter. Alternatively, a small correction of the HV level on PMTs will allow to keep the signal amplitudes stable. One shift corresponds to the radiation dose of 1.2 krad or a signal reduction by 10%. The correction of the HV settings takes less than 5 minutes and could be done at least every shift.

### C. The data acquisition system

The current DAQ systems of both calorimeters are based on the FADC250 (250 Msps Flash Analog-to-Digital Converter) designed by JLab and shown in Fig. 18. They allow creation of a dead-time free readout system without significant new expense.

FIG. 18. FADC250 - Jlab 16 channel VME/VXS based 250Msps Flash ADC digitizer

A 21 slot VXS crate supports up to 16 FADC250 modules (256 channels). Fig. 19 shows the standard FADC250 readout system. The VXS crate uses a standard VME CPU as a crate controller to configure and readout the front-end cards using 1Gbps Ethernet (limiting the readout bandwidth to 120MB/s). The TI and SD modules are responsible for receiving and distributing the global DAQ clock and trigger signals to all FADC250 modules so that all FADC250 in the full system (across multiple crates) remain synchronized. The system clock jitter is under 10ps RMS, contributing negligibly to the timing noise typically achievable by the pulses captured by the FADC250 and TDC modules used at Jlab.

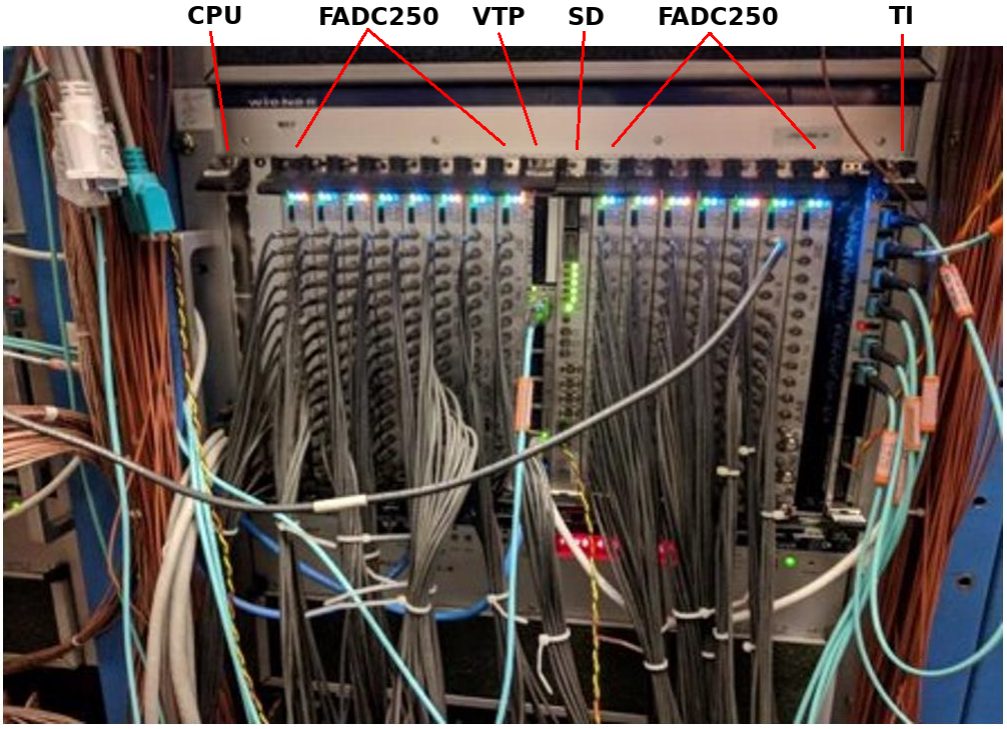


FIG. 19. Jlab VXS Crate of FADC250 modules. CPU is used for readout. VTP for trigger processing. SD to distribute DAQ synchronization signals. TI to receive DAQ synchronization signals from global trigger system.

The VXS Trigger Processor, VTP shown in Fig. 20, collects pulses over the VXS backplane, recorded in the FADC250 to make trigger decisions. The VTP firmware will be configured to perform the FADC250 pulse summation for the electron and proton calorimeters in each sector. Bordering FADC250 channels of sectors can have their information duplicated and forwarded to adjacent crates/VTPs using optical links between VTPs (each VTP has 4 optical links and each can exchange 32 FADC250 channels with the connected VTP). Each VTP for each crate will have an electron trigger and a proton trigger output (asserted when corresponding energy exceeds threshold in regions as defined by trigger requirement). These trigger signals will have programmable latency and width so that an efficient timing coincidence between the proton and electron detectors can be formed. The electron and proton signals will be OR'd together respectively and then these two groups will be AND'd to form the final trigger signal.

The front-end DAQ for the calorimeters is planned to spread across 6 identical crates each corresponding to one sector of the calorimeters. In each of these crate: 11 FADC250 modules will support up to 176 channels of the electron calorimeter NPS crystals, 3 FADC250 modules will support the 48 channels of proton HCAL crystals as shown in Figure 23. This is a standard front-end

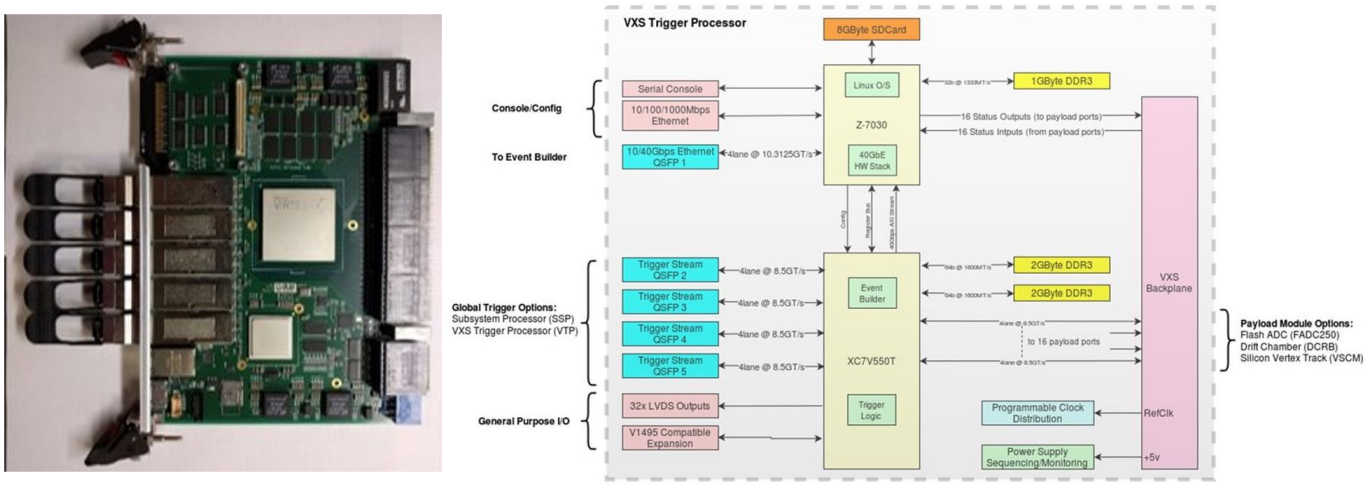


FIG. 20. VTP VXS Module

crate configuration that has been used at Jlab in many experiments to date. These crates will be arranged as shown in Figure 24. The plastic scintillator array will use low-cost, high channel density discriminators and TDCs based on the MAROC3A ASIC. We plan to re-layout the existing Jlab FPGA based MAROC3A readout module used in CLAS12 RICH, shown in Fig. 21, to provide a low cost based hit based readout system. This ASIC and FPGA allow gain normalization of each channel and can operate with a threshold in the single photon region with low noise. Each module contains up to 192 channels. These modules are readout optically using a Jlab Sub System Processor (SSP, showing in Fiber 22), which can readout up to 32 modules. The final system requires two SSP modules, in a VXS crate, with 38 FPGA/ASIC modules. The new layout of the FPGA/ASIC module will have connections to a cable panel for easy connection to the PMTs.

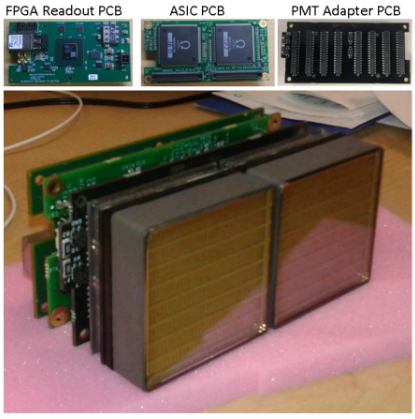


FIG. 21. MAROC3A Readout System used by CLAS12 RICH

### D. Collaboration

The Hall A/C user collaboration consists of members with extensive experience with parity experiments in electron accelerators. In addition, the collaboration includes many individuals from the

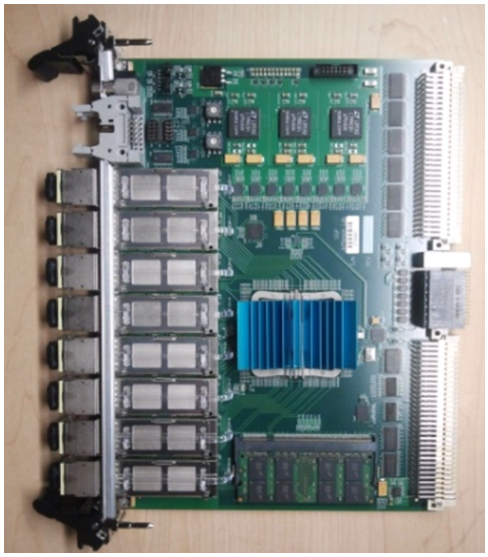

FIG. 22. Jlab Sub System Process (SSP). Used to readout up to 32 MAROC3A FPGA modules (6144 channels)

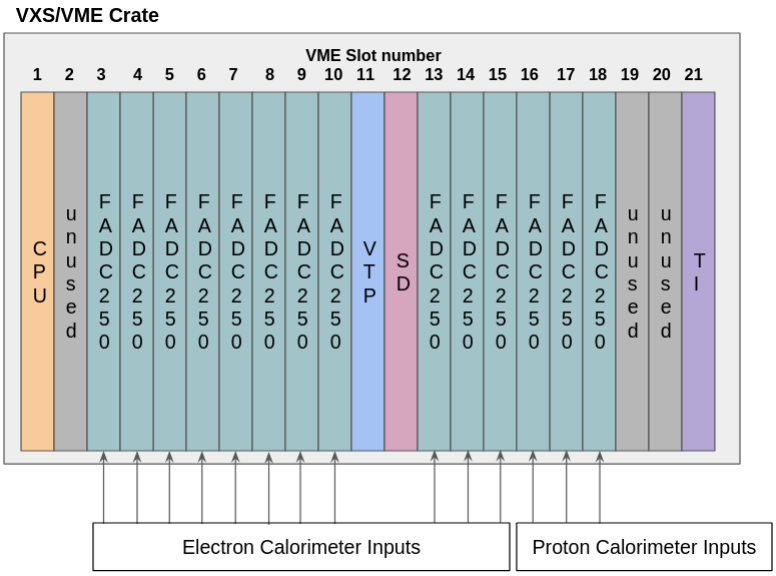


FIG. 23. VXS Crate layout of 1 sector of electron and proton calorimter front-end electronics.

collaborations in Hall A/C with substantial experience in electromagnetic calorimetry and detectors for high energy hadrons.

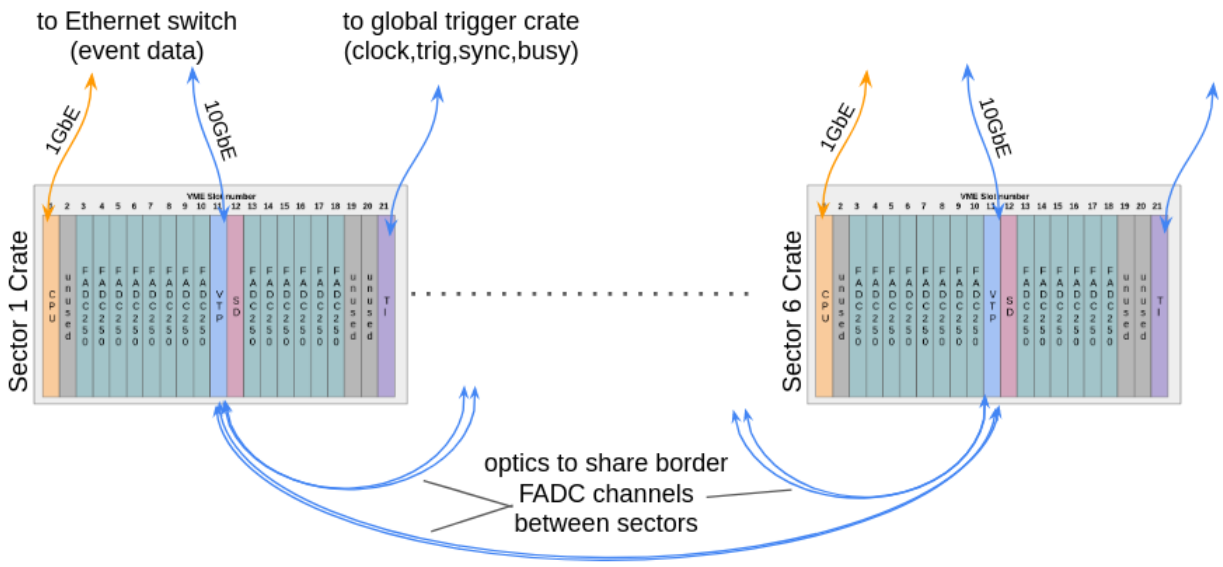


FIG. 24. Layout for 6 sectors proton and electron calorimeter crates. Event readout using 1Gbps Ethernet from the VME CPU (optionally through the VTP 10Gbps Ethernet if needed). VTP optical interconnected to share FADC250 pulse information is supported for energy summation across sectors if needed. Two differential trigger outputs from each VTP, not shown, will go to a simple coincidence logic module (TBD) for the final trigger decision.

## VIII. EXPECTED RESULTS AND BEAM TIME REQUEST

### A. Expected Results

The purpose of this experiment is to measure the $A_{PV}$ with an accuracy sufficient to obtain conclusive evidence on SFFs at large momentum transfer. We will design and construct a full system with complete DAQ in about a year. In the production run the physics asymmetry $A_{PV}$ will be measured to a statistical precision of $\pm 6.2$ ppm. Table IV presents a summary of the error contributions. The expected uncertainty of the SFF is $\pm 0.0042\,(\text{stat}) \pm 0.0024\,(\text{syst})$, or $\delta G^s/G_{Dipole} = \pm 0.088(\text{stat}) \pm 0.051(\text{syst})$, where the first value is statistical error and the second value is systematic error.

| quantity | value | contributed uncertainty |
|---|---|---|
| Beam polarization | 85% ± 1% | 1.2% |
| Beam energy | $6.6 + / - 0.003$ GeV | 0.1% |
| Scattering angle | $15.5^\circ \pm 0.03^\circ$ | 0.4% |
| Beam intensity | <100 nm,<10 ppm | 0.2% |
| Backgrounds | < 0.2 ppm | 0.2% |
| $G_E^n/G_M^n$ | $-0.2122 \pm 0.017$ | 0.9% |
| $G_E^p/G_M^p$ | $0.246 \pm 0.0016$ | 0.1% |
| $\sigma_n/\sigma_p$ | $0.402 \pm 0.012$ | 1.2% |
| $G_A^{Zp}/G_{\text{Dipole}}$ | $-0.15 \pm 0.02$ | 0.9% |
| Total systematic uncertainty: | | 2.2% |

TABLE IV. The estimates of contributions to the relative error of $A_{PV}$ result, to be compared to the statistical precision of $\delta(A_{PV})/A_{PV} = 4.1\%$.

### B. Beam Time Request

The proposed experiment will be done at one beam energy of 6.6 GeV with currents up to 65 $\mu$A. A summary of the requested time is shown in Table V. For the production run we have the following periods: three shifts for commissioning of the polarized beam parameters and instrumentation, two shifts for calibration of the calorimeter with e−p elastic events and checkout of the boiling noise of the hydrogen target, one shift for data taking on dummy target. We also request a total of three days during the running period to measure the beam polarization with the Moller polarimeter. Production time is 40 days. The total beam time request in this proposal is 45 days.

| Configuration # | Procedure | Beam current, $\mu$A | time, days |
|---|---|---|---|
| C1 | Beam parameters | 1-70 | 1 |
| C2 | Detector calibration | 10 | 2/3 |
| C3 | Dummy target data | 20 | 1/3 |
| C4 | Moller polarimetery | 1-5 | 3 |
| C5 | $A_{PV}$ data taking | 60 | 40 |
| | Total requested time | | 45 |

TABLE V. The beam time request for the experiment.

## IX. CONCLUSION

We request 45 days of beam time for the measurement of the strange form factor of the proton at $Q^2 = 2.5$ (GeV/$c$)$^2$ in elastic scattering of 6.6 GeV electrons at 15.5°. This experiment will take place in Hall C, utilizing the polarized electron beam, a hadron calorimeter to detect protons, and an electromagnetic calorimeter to detect scattered electrons. This is the first experiment to measure $A_{PV}$ in elastic electron scattering from the proton at $Q^2$ above 1 (GeV/$c$)$^2$. This experiment will be the first to use coincidence between the electron and the recoiled proton to measure the PVA effect.

Knowledge of the strange form factor at large momentum transfer will allow for determination of the size of the strange quark distribution function, which is crucial to the understanding of nucleon structure. We propose to measure $A_{PV}$ to a statistical precision of ±6.2 ppm. The projected statistical uncertainty of the form factor measurement is $\delta(\mathrm{SFF}) = \pm\,0.004$ (the $G_D$ value is 0.048 at $Q^2$ =2.5 (GeV/$c$)$^2$). Such accuracy will allow significant improvement of flavor decomposition of the nucleon form factors, will test the lattice QCD predictions, and may lead to observation of the non-zero SFF.

## X. PAC50 REPORT ON PR12-22-005

There were several issues which PAC50 suggested evaluating (see the full text on the next page):

- "The PAC would like to see the results of a detailed Geant4 simulation of the experiment confirming the claim of low background in the experiment, as the independent TAC report recommended."
  We developed detailed GEANT4 simulation (see Section V in the proposal) and compared it with our previous analytical calculations.

- "In addition, a detailed design of the experimental setup (including electronics and DAQ) should be presented to assess the viability of the measurement."
  We extended description of the front-end electronics and DAQ in Sec. VII.

- "... the PAC is concerned by the lack of several important experimental details in the proposal."
  In preparation of this proposal the Hall C designer prepared a full CAD model of the setup presented in Sec. IV, see Fig. 7.

## PR12-22-005

**Scientific Rating:** N/A

**Recommendation:** Deferred

**Title:** A Search for a Nonzero Strange Form Factor of the Proton at 2.5 $(GeV/c)^2$

**Spokespersons:** R. Beminiwattha, C. Palatchi, K. Paschke, B. Wojtsekhowski (contact)

**Motivation:** The experiment aims at measuring the strange quark contribution to the proton electromagnetic form factors. This is crucial for their flavour decomposition. This compelling physics case is motivated by recent progress in lattice QCD calculations and by phenomenological models highlighting the potential of a measurement at large $Q^2$.

**Measurement and Feasibility:** The experiment proposes to measure the parity violation asymmetry in electron-proton scattering at $Q^2 = 2.5$ $(GeV/c)^2$. For this purpose, modules of the existing HCAL and NPS need to be rebuilt in a very different detector arrangement, and a new scintillator-based hodoscope (a 45700 channel scintillator array read out by fibers and pixel PMTs) needs to be built. Although the setup is very simple from the kinematic point of view and the measurement is largely limited by statistical uncertainty, the PAC is concerned by the lack of several important experimental details in the proposal.

**Issues:** The PAC would like to see the results of a detailed Geant4 simulation of the experiment confirming the claim of low background in the experiment, as the independent TAC report recommended. In addition, a detailed design of the experimental setup (including electronics and DAQ) should be presented to assess the viability of the measurement.

**Summary:** The presented physics case is timely and extremely compelling. However, the PAC has identified a number of critical items especially in the experimental method, which should be addressed to make sure that no hidden technical problems will jeopardize a successful experimental campaign. The PAC strongly encourages the collaboration to address these items in the future.

[1] T. Horn *et al.*, Scintillating crystals for the neutral particle spectrometer in hall c at jlab, Nuclear Instruments and Methods in Physics Research Section A: Accelerators, Spectrometers, Detectors and Associated Equipment **956**, 163375 (2020).

[2] G. Franklin, HCAL-J status (2014), report at SBS collaboration meeting, July, 2014.

[3] R. Beminiwattha, C. Palatchi, K. Paschke, and B. Wojtsekhowski, A search for a nonzero strange form factor of the proton at 2.5 (gev/c)2, proposal to JLab PAC50 (2022).

[4] D. Beck and B. Holstein, Nucleon structure and parity-violating electron scattering, International Journal of Modern Physics E **10**, 1 (2001), https://doi.org/10.1142/S0218301301000381.

[5] F. Maas and K. Paschke, Strange nucleon form-factors, Progress in Particle and Nuclear Physics **95**, 209 (2017).

[6] D. B. Kaplan and M. Aneesh, Strange matrix elements in the proton from neutral-current experiments, Nuclear Physics B **310**, 527 (1988).

[7] R. D. McKeown, Sensitivity of polarized elastic electron-proton scattering to the anomalous baryon number magnetic moment, Physics Letters B **219**, 140 (1989).

[8] D. Beck, Strange-quark vector currents and parity-violating electron scattering from the nucleon and from nuclei, Phys. Rev. D **39**, 3248 (1989).

[9] P. Souder *et al.*, Measurement of parity violation in the elastic scattering of polarized electrons from $^{12}$C, Phys. Rev. Lett. **65**, 694 (1990).

[10] K. Aniol *et al.*, Measurement of the neutral weak form factors of the proton, Phys. Rev. Lett. **82**, 1096 (1999).

[11] D. Armstrong *et al.*, Strange-quark contributions to parity-violating asymmetries in the forward G0 electron-proton scattering experiment, Phys. Rev. Lett. **95**, 092001 (2005).

[12] S. Baunack *et al.*, Measurement of Strange Quark Contributions to the Vector Form Factors of the Proton at Q**2=0.22 (GeV/c)**2, Phys. Rev. Lett. **102**, 151803 (2009), arXiv:0903.2733 [nucl-ex].

[13] G. D. Cates, C. W. de Jager, S. Riordan, and B. Wojtsekhowski, Flavor decomposition of the elastic nucleon electromagnetic form factors, Phys. Rev. Lett. **106**, 252003 (2011).

[14] M. Jones *et al.* (Jefferson Lab Hall A), G(E(p)) / G(M(p)) ratio by polarization transfer in polarized e p —¿ e polarized p, Phys. Rev. Lett. **84**, 1398 (2000), arXiv:nucl-ex/9910005 [nucl-ex].

[15] M. Musolf, T. Donnelly, J. Dubach, S. Pollock, S. Kowalski, and E. Beise, Intermediate-energy semileptonic probes of the hadronic neutral current, Physics Reports **239**, 1 (1994).

[16] C. Prescott *et al.*, Further measurements of parity non-conservation in inelastic electron scattering, Physics Letters B **84**, 524 (1979).

[17] W. Heil *et al.*, Improved limits on the weak, neutral, hadronic axial vector coupling constants from quasielastic scattering of polarized electrons, Nuclear Physics B **327**, 1 (1989).

[18] B. Mueller *et al.* (SAMPLE Collaboration), Measurement of the proton's neutral weak magnetic form factor, Phys. Rev. Lett. **78**, 3824 (1997).

[19] D. Spayde *et al.*, Parity violation in elastic electron-proton scattering and the proton's strange magnetic form factor, Phys. Rev. Lett. **84**, 1106 (2000).

[20] K. Aniol *et al.*, Parity-violating electroweak asymmetry in e-p scattering, Phys. Rev. C **69**, 065501 (2004).

[21] A. Acha *et al.*, Precision measurements of the nucleon strange form factors at Q2 0.1 GeV2, Phys. Rev. Lett. **98**, 032301 (2007).

[22] Y. Zel'dovich, Electromagnetic interaction with parity violation, Sov. Phys. JETP **6**, 1184 (1958), Zhurnal Eksperimental'noi i Teoretischeskoi Fiziki, 33 (1957) 1531.

[23] S.-L. Zhu, S. Puglia, B. Holstein, and M. Ramsey-Musolf, Nucleon anapole moment and parity-violating ep scattering, Phys. Rev. D **62**, 033008 (2000).

[24] Z. Ye, J. Arrington, R. J. Hill, and G. Lee, Proton and Neutron Electromagnetic Form Factors and Uncertainties, Phys. Lett. B **777**, 8 (2018), arXiv:1707.09063 [nucl-ex].

[25] S. Riordan *et al.*, Measurements of the electric form factor of the neutron up to $Q^2$=3.4 GeV$^2$ using the reaction He-3$(e, e'n)pp$, Phys. Rev. Lett. **105**, 262302 (2010).

[26] M. Diehl and P. Kroll, Nucleon form factors, generalized parton distributions and quark angular momentum, Eur. Phys. J. C **73**, 2397 (2013).

[27] M. E. Christy *et al.*, Form Factors and Two-Photon Exchange in High-Energy Elastic Electron-Proton Scattering, Phys. Rev. Lett. **128**, 102002 (2022), arXiv:2103.01842 [nucl-ex].

[28] C. Chen, C. Fischer, C. Roberts, and J. Segovia, Form factors of the nucleon axial current, Physics Letters B **815**, 136150 (2021).

[29] C. Roberts, private communication (2022).

[30] C. Roberts, Hadron structure using continuum schwinger function methods (2023).

[31] C. Alexandrou *et al.* (Extended Twisted Mass Collaboration), Nucleon axial and pseudoscalar form factors from lattice qcd at the physical point, Phys. Rev. D **103**, 034509 (2021).

[32] J. Xiangdong, Deeply virtual Compton scattering, Phys. Rev. D **55**, 7114 (1997).

[33] A. Radyushkin, Scaling limit of deeply virtual compton scattering, Physics Letters B **380**, 417 (1996).

[34] M. Guidal, M. Polyakov, A. Radyushkin, and M. Vanderhaeghen, Nucleon form factors from generalized parton distributions, Phys. Rev. D **72**, 054013 (2005).

[35] M. Goncharov *et al.*, Precise measurement of dimuon production cross sections in $\nu_\mu$Fe and $\overline{\nu}_\mu$Fe deep inelastic scattering

at the fermilab tevatron, Phys. Rev. D **64**, 112006 (2001).
[36] T. Hobbs, M. Alberg, and G. A. Miller, Constraining nucleon strangeness, Phys. Rev. C **91**, 035205 (2015).
[37] T. Hobbs and G. A. Miller, private communication (2019).
[38] B. Reydo, Trigger with fADC-based systems (2022).
[39] S. Agostinelli *et al.*, Geant4—a simulation toolkit, Nuclear Instruments and Methods in Physics Research Section A: Accelerators, Spectrometers, Detectors and Associated Equipment **506**, 250 (2003).
[40] J. J. Kelly, Simple parametrization of nucleon form factors, Phys. Rev. C **70**, 068202 (2004).
[41] R. Ent, B. W. Filippone, N. C. R. Makins, R. G. Milner, T. G. O'Neill, and D. A. Wasson, Radiative corrections for $(e, e^{'}p)$ reactions at gev energies, Phys. Rev. C **64**, 054610 (2001).
[42] P. M. Nadolsky, H.-L. Lai, Q.-H. Cao, J. Huston, J. Pumplin, D. Stump, W.-K. Tung, and C. P. Yuan, Implications of CTEQ global analysis for collider observables, Phys. Rev. D **78**, 013004 (2008), arXiv:0802.0007 [hep-ph].
[43] M. E. Christy and P. E. Bosted, Empirical fit to precision inclusive electron-proton cross sections in the resonance region, Phys. Rev. C **81**, 055213 (2010).
[44] A. Danagoulian, Measurements of Compton scattering on the proton at 2-6 gev (2006), ph.D. theis, UIUC.
[45] A. Danagoulian *et al.*, Compton-scattering cross section on the proton at high momentum transfer, Phys. Rev. Lett. **98**, 152001 (2007).
[46] D. Wang *et al.* (PVDIS), Measurement of parity violation in electron–quark scattering, Nature **506**, 67 (2014).
[47] A. Boyarski *et al.*, Photoproduction of k+ -hyperon from hydrogen and deuterium at 11 gev, Physics Letters B **34**, 547 (1971).
[48] D. Carman *et al.* (CLAS Collaboration), Beam-recoil polarization transfer in the nucleon resonance region in the exclusive $\vec{e}\ p \to e^{'} K^{+} \vec{\Lambda}$ and $\vec{e}\ p \to e^{'} K^{+} \vec{\Sigma}^{0}$ reactions at the clas spectrometer, Phys. Rev. C **79**, 065205 (2009).
[49] P. Monaghan, CDET status (2016), report at SBS collaboration meeting, July, 2016.
[50] V. Batarin *et al.*, Study of radiation damage in lead tungstate crystals using intense high-energy beams, Nuclear Instruments and Methods in Physics Research Section A: Accelerators, Spectrometers, Detectors and Associated Equipment **512**, 488 (2003).
[51] V. Dormenev *et al.*, Stimulated recovery of the optical transmission of pbwo4 scintillation crystals for electromagnetic calorimeters after radiation damage, Nuclear Instruments and Methods in Physics Research Section A: Accelerators, Spectrometers, Detectors and Associated Equipment **623**, 1082 (2010).